

## A Direct Sampling Method for the Inversion of the Radon Transform\*

Yat Tin Chow<sup>†</sup>, Fuqun Han<sup>‡</sup>, and Jun Zou<sup>‡</sup>

**Abstract.** We propose a novel direct sampling method (DSM) for the effective and stable inversion of the Radon transform. The DSM is based on a generalization of the important almost orthogonality property in classical DSMs to fractional order Sobolev duality products and to a new family of probing functions. The fractional order duality product proves to be able to greatly enhance the robustness of the reconstructions in some practically important but severely ill-posed inverse problems associated with the Radon transform. We present a detailed analysis to better understand the performance of the new probing and index functions, which are crucial to stable and effective numerical reconstructions. The DSM can be computed in a very fast and highly parallel manner. Numerical experiments are carried out to compare the DSM with a popular existing method and to illustrate the efficiency, stability, and accuracy of the DSM.

**Key words.** inverse problem, radon transform, direct sampling method, imaging technique

**AMS subject classifications.** 44A12, 65R32, 92C55, 94A08

**DOI.** 10.1137/20M1374997

**1. Introduction.** In this work, we consider the inverse problem of recovering a function from its Radon transform. This problem arises when we aim at recovering an object from its projections in computed tomography (CT). Accurate, stable, and fast numerical reconstruction methods are of great importance in practice in view of the broad and increasing applications of CT scan in, e.g., medical imaging, flaw detection, and baggage security scanning.

To recover a function from its Radon transform, analytical inversion formulas are available. And some popular approaches nowadays are based on these formulas along with various low pass filters, known as filtered back projections (FBP). Two major reasons for the popularity of the FBP method are its easy implementation and its relatively low computational complexity [29]. The method performs very well when the measurement data is very accurate and available from all directions. Nonetheless, the measurement data may be highly noisy and is only available in a limited range or only a number of angles in many applications. For instance, to minimize adverse effects brought by radiation exposure upon a patient's body during the scanning process, low dose CT is widely employed for lung cancer detection [36]. However, this may lead to severely polluted measurement data [26], and in this case, it is difficult for traditional noniterative methods, such as FBP methods and Fourier methods [27], to work

\*Received by the editors October 26, 2020; accepted for publication (in revised form) April 19, 2021; published electronically July 19, 2021.

<https://doi.org/10.1137/20M1374997>

**Funding:** The work of the first author was supported by Omnibus Research and Travel Award and a startup grant from University of California, Riverside. The work of the third author was supported by Hong Kong RGC General Research Fund projects 14306718, 14304517.

<sup>†</sup>Department of Mathematics, University of California, Riverside, Riverside, CA 92521 USA ([yattinc@ucr.edu](mailto:yattinc@ucr.edu)).

<sup>‡</sup>Department of Mathematics, Chinese University of Hong Kong, Shatin, N.T., Hong Kong, China ([fqhan@math.cuhk.edu.hk](mailto:fqhan@math.cuhk.edu.hk), [zou@math.cuhk.edu.hk](mailto:zou@math.cuhk.edu.hk)).

stably, which will be demonstrated in our subsequent numerical experiments. Another instance is when we apply the CT scan in luggage security checks, where we may only be able to collect measurement data from a small number of or/and a limited range of angles. Those scenarios are usually named sparse tomography and limited angle tomography, and the singular values of the corresponding forward operator decay faster [11]. Therefore, by one definition that states that the ill-posedness of the problem depends on the decaying rate of singular values in [38], the inverse problems that we are interested in are severely ill-posed and sensitive to noise. It is challenging to develop efficient and effective reconstruction methods in these special scenarios.

Due to wide applications of the inversion of the Radon transform, many efficient numerical methods are proposed. They can be generally classified into two categories, direct (noniterative) methods and iterative methods. Direct methods are usually based on a mathematically exact inversion formula, which include FBP methods that apply various low pass filters on the measurement data [22, 27, 28] and Fourier methods that implement certain inversion formulas in the Fourier domain [27, 33]. Direct methods are usually easy to implement and fast to compute, but it is difficult for them to provide high quality reconstruction results with limited and noisy measurement data. For iterative methods, algebraic reconstruction type methods derived from the Kaczmarz method [2, 15] and expectation minimization methods for maximizing likelihood functions [18, 34] have been widely applied since the last century. A comprehensive review of those traditional iterative methods can be found in [3]. Recently, iterative methods to minimize a cost functional with a data matching term and certain regularization become popular for the case that measurement data is noisy and relatively sparse. These methods include standard total variation (TV) regularization [4, 12, 32], nonconvex minimization for  $L^p$  TV regularization (with  $p < 1$ ) to improve the reconstruction under limited measurements [5], and anisotropic TV minimization for limited angle tomography [7]. Moreover, the regularization term can also be derived from a certain norm of wavelet coefficients [16, 31], and Bayesian methods with nonlocal prior information [6].

We would like to remark that since the above iterative type algorithms usually involve more advanced mathematical or statistical tools, they may employ either certain optimization functional or leverage on the availability of a huge training dataset, which may lead to higher computational and storage complexities than direct methods. Instead, we will propose a method that avoids high computational and storage complexities and at the same time obtains a reasonable reconstruction in these difficult scenarios. In particular, the direct and iterative methods can be combined; for instance, the proposed direct sampling method (DSM) can be used as an initial estimate for many iterative methods to reduce the number of iterations required, which are demonstrated in the subsequent numerical experiments.

In this work, we design a novel DSM for the inversion of the Radon transform. This type of method was originally motivated by a crucial observation which is referred to as the almost orthogonality property. The property associated with an inverse problem may be stated roughly as follows: for a Sobolev duality product  $\langle \cdot, \cdot \rangle$ , the function  $K(x, z) := \langle G_x, \eta_z \rangle$  defined for a fundamental solution  $G_x$  at point  $x$  and a probing function  $\eta_z$  at point  $z$  behaves like a Gaussian distribution, i.e.,  $K(x, z)$  achieves the maximum at  $z = x$  and decays quickly when  $z$  moves away from  $x$ . This property was a key observation and motivation in the development of the previous DSMs. The DSMs have been constructed and developed for various highly nonlinear and severely ill-posed inverse problems (see, e.g., [8, 9, 10, 19, 25, 30]), including the

wave and nonwave type inverse problems. These developments have demonstrated that the DSMs are robust against noise and could generate reasonable reconstruction results even with highly limited measurement data. These attractive features motivate us naturally to design a DSM for inverting the Radon transform, and this is the main focus of the current work. A key observation in our development is that if the measurement data is directly back-projected by the dual of the Radon transform, the result can be represented by an integral equation with the Green's function associated with (a fractional) Laplacian as its kernel. This suggests making full use of the important almost orthogonality property between the Green's function and a special family of probing functions under a fractional order Sobolev duality product. The choice of the fractional order operator arises naturally considering the ill-posedness of the inverse problem under noisy and incomplete measurement data and turns out to be able to greatly enhance the robustness of the new DSM. In the meantime, in order to generate more satisfactory reconstruction results, we introduce the probing functions that depend on the sampling interval, which can further render a pointwise convergence of the index function in certain scenarios. From the perspective of the numerical computations, the DSM can be computed with low computational efforts and simultaneously with the measurement process. With these features, the new DSM is expected to find applications in tackling some inverse problems associated with the Radon transform, such as those arising from security scanning, cancer detection, and portable CT scanners. These will be further verified numerically in section 6.

The rest of the paper runs as follows. Section 2 introduces basic motivations and principles behind direct sampling type methods for the inversion of the Radon transform, including our detailed choices of probing and index functions. Section 3 provides mathematical justifications for the novel DSM and investigates how the choice of some critical parameters in the sampling algorithm affects the reconstruction. Section 4 extends the newly proposed DSM to the limited angle tomography and the exponential Radon transform. Section 5 presents some strategies for the numerical implementation to enhance the robustness and reduce the computational complexity of the new DSM. Section 6 demonstrates a series of numerical experiments by the new sampling method for some highly ill-posed scenarios, along with a comparison with the popular FBP method and regularization type methods.

**2. Principles of DSMs in inverting the Radon transform.** In this section, we explain the basic principles of direct sampling type methods for the inversion of the Radon transform. The spirit of direct sampling type methods is to leverage upon an almost orthogonality property between the family of fundamental solutions of the forward problem and a set of probing functions under an appropriately chosen duality product [8, 9, 10]. With this in mind, we first represent the measurement data with the Green's function of (a fractional) Laplacian and then introduce a fractional order Sobolev duality product for the coupling of the measurement data and the probing function. At the same time, a family of probing functions will be constructed. Finally, an index function is defined to generate a DSM for the inversion of the Radon transform.

Let us consider the target function to be recovered as  $f$ , which is compactly supported in  $\Omega$  and contained in  $L^\infty(\Omega)$ , where  $\Omega$  is a compact set in  $\mathbb{R}^n$  ( $n = 2, 3$ ). Moreover, we assume  $B(0, r_1) \subseteq \Omega \subseteq B(0, r_2)$ , with  $0 < r_1 \leq r_2$ , where  $B(x, r)$  is the ball centered at  $x$  with radius

$r$ . The Radon transform of a function  $f$  and its dual acting on a function  $g \in L^\infty(S^{n-1} \times \mathbb{R})$  are defined respectively by

$$(2.1) \quad Rf(\theta, t) := \int_{x \cdot \theta = t} f(x) dx_L = \int_{\mathbb{R}^n} f(x) \delta(t - x \cdot \theta) dx, \quad R^*g(x) := \int_{S^{n-1}} g(\theta, x \cdot \theta) d\theta,$$

where  $\theta \in S^{n-1}$ ,  $t \in \mathbb{R}$ ,  $x \in \Omega$ , and  $t = x \cdot \theta$  represents a hyperplane with normal direction  $\theta$  and distance  $t$  to the origin. We shall first focus on the case that  $Rf(\theta, t)$  is available for all  $\theta \in S^{n-1}$  and for all  $t \in I_\theta$ , where  $I_\theta$  is defined such that

$$(2.2) \quad \Omega \subset \bigcup_{t \in I_\theta} \{x : t = x \cdot \theta\}.$$

In other words, we have measurements for all hyperplanes that intersect with the convex hull of  $\Omega$ . In section 4, we shall further consider the application of DSM for reconstruction with limited angle measurement, i.e.,  $t$  is available only for a subset of  $I_\theta$ .

A crucial motivation in our subsequent design of a DSM is the following inherent mathematical connection between the Radon transform and (a fractional) Laplacian [17, p. 9]:

$$(2.3) \quad R^*Rf(x) = \frac{c_n}{d_n} \int_{\Omega} f(y) G_x(y) dy \quad \text{with } d_n = \frac{\pi^{1/2}}{(4\pi)^{\frac{n-1}{2}} \Gamma(\frac{n}{2})} \quad \text{and } c_n = \frac{\Gamma(\frac{n-1}{2})}{2\pi^{\frac{n+1}{2}}},$$

where  $G_x(y) = |x - y|^{-1}$  is the Green's function for the (fractional) Laplacian operator  $(-\Delta)^{(n-1)/2}$ . We use the definition of the fractional Laplacian in  $\mathbb{R}^n$  by the Fourier multiplier. More specifically, for a given target function  $f \in C_c^\infty(\Omega)$ , we first extend it by zero to obtain  $f \in C_c^\infty(\mathbb{R}^n)$ , then perform its Fourier transform in  $\mathbb{R}^n$  and multiply the result with a Fourier multiplier  $|\xi|^{2\gamma}$ , and then take the inverse Fourier transform in  $\mathbb{R}^n$  to compute  $(-\Delta)^\gamma f$ . This definition of the fractional Laplacian for  $f \in C_c^\infty(\Omega)$  can be quickly generalized to tempered distributions in  $\mathbb{R}^n$  in the standard manner. Our definition does not consider a spectral decomposition of the Laplacian over  $\Omega$  with a choice of boundary condition (e.g., Dirichlet or Neumann). Moreover, various definitions of the fractional Laplacian in [23] are equivalent to the definition we use through a Fourier multiplier.

The following equivalent inversion formula will be frequently used in our subsequent analysis:

$$(2.4) \quad f(x) = (-\Delta)^{\frac{(n-1)}{2}} u_s(x) \quad \text{with } u_s(x) := d_n R^*Rf(x).$$

We shall call  $u_s$  the measurement data since the dual transform or the back projection  $R^*$  of the Radon transform is standard and explicitly available after the Radon transform  $Rf(\theta, t)$ .

The relation (2.4) can be considered as the most important motivation for many existing reconstruction methods, e.g., the FBP and Fourier methods. These reconstruction methods involve usually the application of a pseudodifferential operator on the noisy measurement data which is not preferable for those ill-posed scenarios that were mentioned in the introduction.

We remark that in order to allow (2.4) to be held in  $\mathbb{R}^2$ , we shall assume that  $f$  lies in the Schwarz space, which is the space of functions whose derivatives are all rapidly decreasing. This assumption will not affect the feasibility of reconstructing the target function  $f \in L^\infty(\Omega)$ .

Using the density of smooth functions in  $L^\infty(\Omega)$ , all our upcoming analyses involving (2.4) (section 3) can be first carried out for smooth functions, and then extended to a more general class of target functions by a standard density argument.

To define an index function that is crucial to a DSM, we introduce a Sobolev duality product of order  $\gamma > 0$ :

$$(2.5) \quad \langle v, w \rangle_\gamma := \int_{\mathbb{R}^n} v (-\Delta)^\gamma w dx \quad \forall v \in L^2(\mathbb{R}^n), w \in H^{2\gamma}(\mathbb{R}^n).$$

The two arguments  $v$  and  $w$  above will often be the noisy measurement data and the probing functions (to be defined) in our proposed DSM. The name of the Sobolev duality product comes from the following reasoning: First, we notice that the completion of  $H^{2\gamma}(\mathbb{R}^n)$  under the seminorm  $|\cdot|_{2\gamma} := \sqrt{\langle (-\Delta)^\gamma \cdot, (-\Delta)^\gamma \cdot \rangle_{L^2(\mathbb{R}^n)}}$  is a Hilbert space. The seminorm  $|\cdot|_{2\gamma}$  is actually a norm since a function that is weakly harmonic implies it is harmonic and the only  $2\gamma$ -harmonic function in  $H^{2\gamma}(\mathbb{R}^n)$  is 0 [13]. We write this completed space as  $\mathcal{H} := \overline{H^{2\gamma}(\mathbb{R}^n)}^{|\cdot|_{2\gamma}}$ , which contains  $H^{2\gamma}(\mathbb{R}^n)$  a strict subspace. Then we can rigorously show that the dual space  $\mathcal{H}^*$  of  $\mathcal{H}$  (that is itself isomorphic to  $\mathcal{H}$  via Riesz representation) is also isomorphic to  $L^2(\mathbb{R}^n)$  via the mapping  $v \in L^2(\mathbb{R}^n) \mapsto \langle v, \cdot \rangle_\gamma \in \mathcal{H}^*$ . With this notion in mind, we call (2.5) a duality product between  $\mathcal{H}$  and its dual space  $\mathcal{H}^*$  (identified as  $L^2(\mathbb{R}^n)$ ). For our subsequent analysis of DSM, we will restrict our attention to the case that  $w \in H^{2\gamma}(\mathbb{R}^n)$  and call the parameter  $\gamma$  in (2.5) the Sobolev scale of the duality product.

The new DSM will rely on a critical index function, which involves an appropriately selected family of probing functions. Before going on with more details, we first present one of the primary motivations for employing the duality product in (2.5) and the construction of probing functions for the inversion of the Radon transform. Let us consider  $n = 2$ , and choose  $w = u_s$  from (2.4),  $v = G_z$ , and Sobolev scale  $\gamma = 1$  in (2.5). Then we can easily derive by the definition of the Green's function and the inversion formula in (2.4) that

$$(2.6) \quad \langle u_s, G_z \rangle_1 = \int_{\mathbb{R}^n} (-\Delta) G_0(z-x) u_s(x) dx = ((-\Delta) G_0 * u_0)(z) = \mathcal{F}^{-1}\{|\omega| \mathcal{F}(f) \mathcal{F}(G_0)\}(z) = f(z),$$

where  $\mathcal{F}$  and  $\mathcal{F}^{-1}$  denote the Fourier inverse Fourier transforms, and  $\omega$  is the variable in the frequency domain. Therefore, the duality product defined in (2.5) between  $u_s$  and the Green's function  $G_z$  can be linked with an exact reconstruction formula. However, we may directly observe that taking the Laplacian on  $u_s$  will cause numerical instability due to the noise in the data, especially in those scenarios we mentioned in the introduction. Furthermore, essentially different from the previous DSMs [8, 9, 10] for which the measurement data is collected on a partial boundary of the sampling domain, we now have the data  $u_s$  inside  $\Omega$ . Hence, it is not desirable in practice for our numerical methods to involve the singularity of the Green's function (as in (2.6)) in computations. For this reason, we shall introduce and justify the following strategies (in sections 2.1 and 3):

- To enhance the robustness against noise, a smaller Sobolev scale  $\gamma$  in the duality product will be preferable when the measurement data is highly noisy. Moreover, we will illustrate in section 3 the relationship between  $\gamma$  and the variance of the index function under a simplified noise model.

- We will introduce a special family of probing functions to avoid any singularities at the sampling point  $z$  but still preserve the sharpness of the inversion formula.

**2.1. Probing and index functions.** We are now going to propose an appropriate family of probing functions based on the primary motivation and principles of direct sampling type methods that we addressed earlier. For that purpose, we first define two sets of auxiliary functions  $\zeta_\alpha^h$  and  $\tilde{\zeta}_\alpha^h$  for any  $0 < h < 1$  and  $\alpha > 0$ :

$$(2.7) \quad \zeta_\alpha^h(x) := \begin{cases} |x|^{-\alpha} & \text{when } |x| \geq h, \\ \psi_\alpha(|x|) & \text{when } |x| < h; \end{cases} \quad \tilde{\zeta}_\alpha^h(x) := \begin{cases} |x|^{-\alpha} & \text{when } |x| \geq h, \\ h^{-\alpha} & \text{when } |x| < h; \end{cases}$$

where  $\psi_\alpha(x)$  is a smooth extension function such that  $\zeta_\alpha^h(x) \in C^{2,1}(\mathbb{R}^n)$  and  $\|\zeta_\alpha^h - \tilde{\zeta}_\alpha^h\|_{L^1(\mathbb{R}^n)} < h$ . By the density of smooth functions in  $L^2(\mathbb{R}^n)$ , we will present an explicit choice of the smooth extension function  $\psi_\alpha$  that we use in our numerical computations with verification of its desired property in Appendix A.

In what follows,  $\zeta_\alpha^h$  is used to construct a crucial family of probing functions, and  $\tilde{\zeta}_\alpha^h$  will be repeatedly employed in the theoretical justification of the DSM in section 3. These auxiliary functions can be regarded as some delicate modifications of the Green’s function associated with the (fractional) Laplacian  $(-\Delta)^{(n-1)/2}$ . The modifications are necessary for two reasons. The first is that the original Green’s function is singular at the origin, therefore we need to remove the singularity but still preserve a certain smoothness property. Second, a key parameter  $\alpha$  is introduced to realize a more satisfactory reconstruction result. Indeed, we will justify in section 3.2 that a reasonable and reliable choice is  $\alpha = n + 1$ .

We are now ready to define a crucial family of probing functions  $\eta_z^h$  at any sampling point  $z \in \Omega$ :

$$(2.8) \quad \eta_z^h(x) := \zeta_{n+1}^h(x - z).$$

For notational reasons, we also denote

$$(2.9) \quad \tilde{\eta}_z^h(x) := \tilde{\zeta}_{n+1}^h(x - z).$$

Before we move on to introduce the important index function for defining the DSM, we first provide some estimates of probing functions, which will be used repeatedly in the verification of the new DSM in section 3. We would like to point out that Lemma 2.1 can be proved also by using the Hölder estimate [35] and Sobolev embedding theorems. We still provide an alternative but more direct proof for both the completeness and the subsequent analysis.

**Lemma 2.1.** *The following estimates hold for the probing and auxiliary functions  $\eta_z^h$  and  $\tilde{\eta}_z^h$ :*

- (a)  $(-\Delta)^\gamma \eta_z^h(x)$  belongs to  $L^\infty(\mathbb{R}^n)$  for  $0 < \gamma < \frac{n}{2}$ ;
- (b)  $(-\Delta)^\gamma \eta_z^h(x)$  belongs to  $L^2(\mathbb{R}^n)$  for  $0 < \gamma < 1$ ;
- (c)  $(-\Delta)^\gamma \tilde{\eta}_z^h(x)$  belongs to  $L^2(\mathbb{R}^n)$  for  $0 < \gamma < 1$ .

*Proof.* Without loss of generality, we assume that  $z$  is the origin.

To show part (a), we first consider the case  $\gamma \in (0, 1)$ . By definition, the fractional Laplacian of  $\eta_0^h$  for an arbitrary point  $x \in \mathbb{R}^n$  can be written as

$$(2.10) \quad \begin{aligned} (-\Delta)^\gamma \eta_0^h(x) &= -\frac{c_{n,\gamma}}{2} \lim_{\delta \rightarrow 0} \int_{|y|>\delta} \frac{\eta_0^h(x+y) + \eta_0^h(x-y) - 2\eta_0^h(x)}{|y|^{n+2\gamma}} dy \\ &= -\frac{c_{n,\gamma}}{2} (I_1 + I_2) \quad \text{with } c_{n,\gamma} = \frac{4^\gamma \Gamma(\frac{n}{2} + \gamma)}{\pi^{n/2} |\Gamma(-\gamma)|}, \end{aligned}$$

where  $I_1$  and  $I_2$  are

$$I_1 = \int_{|y|>\frac{|x|}{2}} \frac{\eta_0^h(x+y) + \eta_0^h(x-y) - 2\eta_0^h(x)}{|y|^{n+2\gamma}} dy, \quad I_2 = \lim_{\delta \rightarrow 0} \int_{\delta < |y| < \frac{|x|}{2}} \frac{\eta_0^h(x+y) + \eta_0^h(x-y) - 2\eta_0^h(x)}{|y|^{n+2\gamma}} dy.$$

$I_1$  can be bounded directly by

$$(2.11) \quad |I_1| \leq \int_{|y|>\frac{|x|}{2}} \frac{|\eta_0^h(x+y) + \eta_0^h(x-y) - 2\eta_0^h(x)|}{|y|^{n+2\gamma}} dy \leq 4 \|\eta_0^h\|_{L^1(\mathbb{R}^n)} |x/2|^{-n-2\gamma},$$

while  $I_2$  can be bounded by

$$(2.12) \quad |I_2| \leq \lim_{\delta \rightarrow 0} \int_{\delta < |y| < \frac{|x|}{2}} \frac{\|D^2 \eta_0^h\|_{L^\infty(B(x, |x|/2))}}{|y|^{n+2\gamma-2}} dy \leq c_2(n, \gamma) \|D^2 \eta_0^h\|_{L^\infty(B(x, |x|/2))} |x/2|^{2-2\gamma},$$

by using the estimate

$$(2.13) \quad \frac{|\eta_0^h(x+y) + \eta_0^h(x-y) - 2\eta_0^h(x)|}{|y|^{n+2\gamma}} \leq \frac{\|D^2 \eta_0^h\|_{L^\infty(B(x, |x|/2))}}{|y|^{n+2\gamma-2}}, \quad \text{where } |y| < \frac{|x|}{2},$$

from the second order Taylor's theorem. Here the constant  $c_2(n, \gamma)$  only depends on  $n$  and  $\gamma$ . Combining (2.11) and (2.12), we conclude that  $(-\Delta)^\gamma \eta_0^h \in L^\infty(\mathbb{R}^n)$  for  $\gamma \in (0, 1)$ .

Now we show  $(-\Delta)^\gamma \eta_z^h(x) \in L^\infty(\mathbb{R}^n)$  for  $\gamma \in [1, \frac{n}{2})$ . We first establish a result that will be used twice in the following proof. For arbitrary  $g \in C^{0,1}(\mathbb{R}^n) \cap L^\infty(\mathbb{R}^n)$  and  $\beta \in (0, 1/2)$ , we have

$$(2.14) \quad \begin{aligned} |(-\Delta)^\beta g(x)| &\leq c_{n,\beta} \left[ \int_{B(0,1)} \frac{\|g\|_{C^{0,1}(\mathbb{R}^n)}}{|y|^{n+2\beta-1}} dy + \int_{\mathbb{R}^n \setminus B(0,1)} \frac{2\|g\|_{L^\infty(\mathbb{R}^n)}}{|y|^{n+2\beta}} dy \right] \\ &\leq c_3(n, \beta) (\|g\|_{C^{0,1}(\mathbb{R}^n)} + \|g\|_{L^\infty(\mathbb{R}^n)}) \end{aligned}$$

for  $c_{n,\beta}$  defined in (2.10) and some constant  $c_3(n, \beta)$  that only depends on  $n$  and  $\beta$ . The above estimate implies  $(-\Delta)^\beta g \in L^\infty(\mathbb{R}^n)$  for any  $g \in C^{0,1}(\mathbb{R}^n) \cap L^\infty(\mathbb{R}^n)$  and  $\beta \in (0, 1/2)$ .

Next, by the construction of the probing function in (2.8), we have  $(-\Delta)\eta_0^h \in C^{0,1}(\mathbb{R}^n) \cap L^\infty(\mathbb{R}^n)$ , which shows the case  $\gamma = 1$ . For  $\gamma > 1$ , to make use of the estimate in (2.14), we observe that the order  $\gamma$  fractional Laplacian of the probing function can be written as

$$(-\Delta)^\gamma \eta_0^h = (-\Delta)^{\gamma-1} ((-\Delta)\eta_0^h) \quad \text{with } \gamma \in \left(1, \frac{n}{2}\right).$$

This indicates  $(-\Delta)^\gamma \eta_0^h \in L^\infty(\mathbb{R}^n)$  by replacing  $g$  by  $(-\Delta)\eta_0^h$  and  $\beta$  by  $\gamma - 1 \in (0, 1/2)$  in (2.14).

To show part (b) that  $(-\Delta)^\gamma \eta_0^h \in L^2(\mathbb{R}^n)$  for  $\gamma \in (0, 1)$ , it suffices to show that  $|(-\Delta)^\gamma \eta_0^h(x)| \leq c|x|^{-n-\epsilon}$  for  $|x| > 2h$ ,  $\epsilon > 0$ , and some constant  $c$  that is independent of  $x$ . This property is satisfied by  $I_1$  due to (2.11). Now we investigate  $I_2$  in (2.10) more carefully. By the definition of the probing function, we have

$$(2.15) \quad \|D^2 \eta_0^h\|_{L^\infty(B(x, |x|/2))} \leq 4n^2|x/2|^{-n-3} \quad \text{when } |x| > 2h.$$

Substituting this estimate into (2.12) implies that  $|I_2| \leq c_2(n, \gamma)4n^2|x/2|^{-n-1-2\gamma}$ . Hence, we can conclude that  $(-\Delta)^\gamma \eta_0^h \in L^2(\mathbb{R}^n)$ .

To show part (c) that  $(-\Delta)^\gamma \tilde{\eta}_0^h \in L^2(\mathbb{R}^n)$  for  $\gamma \in (0, 1)$ , we first notice that for  $|x| > 2h$ , all above estimates in (2.11), (2.12), and (2.15) hold after replacing  $\eta_0^h$  by  $\tilde{\eta}_0^h$  since the pointwise value of  $\tilde{\eta}_0^h(x)$  for  $|x| < h$  is not involved in those estimations. Therefore, we have  $(-\Delta)^\gamma \tilde{\eta}_0^h \in L^2(\mathbb{R}^n \setminus B(0, 2h))$ . Now, it only remains to show  $(-\Delta)^\gamma \tilde{\eta}_0^h$  belongs to  $L^2(B(0, 2h))$ .

For  $\gamma \in (0, 1/2)$ , with (2.14) and the definition in (2.7) which states that  $\tilde{\eta}_0^h \in C^{0,1}(\mathbb{R}^n)$ , we have  $(-\Delta)^\gamma \tilde{\eta}_0^h \in L^\infty(B(0, 2h)) \subset L^2(B(0, 2h))$ .

For  $\gamma \in [1/2, 1)$ , denoting  $\bar{\eta}_0^h := \eta_0^h - \tilde{\eta}_0^h$  which satisfies  $\bar{\eta}_0^h(x) = 0$  if  $|x| > h$ . Then showing  $(-\Delta)^\gamma \tilde{\eta}_0^h$  belongs to  $L^2(B(0, 2h))$  is equivalent to showing  $(-\Delta)^\gamma \bar{\eta}_0^h$  belongs to  $L^2(B(0, 2h))$ . By definition, for  $h < |x| < 2h$ , we have

$$|(-\Delta)^\gamma \bar{\eta}_0^h(x)| = c_{n,\gamma} \left| \int_{|y| < h} \frac{\bar{\eta}_0^h(y)}{|x-y|^{n+2\gamma}} dy \right| \leq 4\pi^2 c_{n,\gamma} \|\eta_0^h - \tilde{\eta}_0^h\|_{L^\infty(\mathbb{R}^n)} (|x| - h)^{-2\gamma}.$$

For  $|x| < h$ , similarly to the decomposition in (2.10), we have

$$\begin{aligned} |(-\Delta)^\gamma \bar{\eta}_0^h(x)| &\leq c_{n,\gamma} \left| \int_{|y| < h-|x|} \frac{\bar{\eta}_0^h(x-y) + \bar{\eta}_0^h(x+y) - \bar{\eta}_0^h(x)}{2|y|^{n+2\gamma}} dy \right| + c_{n,\gamma} \left| \int_{h-|x| < |y| < 2h} \frac{\bar{\eta}_0^h(x) - \bar{\eta}_0^h(x+y)}{|y|^{n+2\gamma}} dy \right| \\ &\leq c_4(n, \gamma) \left[ \|D^2(\eta_0^h - \tilde{\eta}_0^h)\|_{L^\infty(B(0,h))} (h - |x|)^{2-2\gamma} + 2\|\eta_0^h - \tilde{\eta}_0^h\|_{L^\infty(\mathbb{R}^n)} (h - |x|)^{2\gamma} \right] \end{aligned}$$

for some constant  $c_4(n, \gamma)$  that is independent of  $x$ . Combining estimates for  $|x| > h$  and  $|x| < h$ , we conclude that  $(-\Delta)^\gamma \bar{\eta}_0^h \in L^2(B(0, 2h))$ , which leads to part (c) of the lemma. ■

We are now ready to introduce the crucial index function  $I_\gamma^h$  that defines the DSM, more accurately speaking, it generates the numerical image at all sampling points  $z \in \Omega$ :

$$(2.16) \quad I_\gamma^h(z) := \frac{\langle u_s, \eta_z^h \rangle_\gamma}{n(z)} \quad \text{with } n(z) := \langle d_n R^* R(\mathbb{1}_\Omega), \eta_z^h \rangle_\gamma,$$

where  $\eta_z^h$  is the probing function introduced in (2.8) and  $d_n$  is defined in (2.3). The normalization term  $n(z)$  is taken to migrate the influence of the choice of  $h$  and  $\gamma$  on the magnitude of the index function, which is independent of the measurement data  $u_s$ . In particular, this choice of  $n(z)$  ensures that our method is exact for constant valued target function. In sections 3.1 and 3.3, we shall justify that the numerator of the index function, that is, the duality product between  $u_s$  and  $\eta_z^h$ , will approximately recover the target function  $f(z)$  up to a constant. With this in mind, we observe that  $n(z)$  is simply an approximation to the characteristic function of the sampling domain  $\Omega$ , hence  $n(z)$  is nearly a constant for all sampling points in  $\Omega$ .

We remark that, since  $u_s$  introduced in (2.4) is not compactly supported, the duality product involved in the index function (2.16) is defined with respect to  $\mathbb{R}^n$ . However, the numerical implementation of the index function is still realized in a compact set due to the fact that the target function  $f$  is often compactly supported in  $\Omega$ . The implementation of the new DSM will be presented in detail in section 5

The proposed index function leverages upon the very important almost orthogonality property of the Green's function  $G_x$  and the family of probing functions defined in (2.8) in fractional order Sobolev duality products, i.e., the magnitude of  $\langle G_x, \eta_z \rangle_\gamma$  is large when  $z$  is close to  $x$  and decays quickly when  $z$  moves away from  $x$ . Combined with the representation of the measurement data that we introduced in (2.4), this desired property helps reconstruct the target function  $f$  with the index function (see the careful verification in section 3). We now emphasize a very important feature of the novel DSM. By the definition of the index function (2.16), the evaluation of the index function does not involve any pseudodifferential operator applied to the noisy measurement data  $u_s$ , unlike many existing numerical methods in inverting the Radon transform. This feature shall allow our DSM to be stable under high level noise and limited measurement data, which is evident from many numerical experiments in section 6.

Under the setups above, the index function in (2.16) gives rise to our new algorithm.

**Direct sampling method.** Given the Radon transform  $Rf(\theta, t)$  of the target function  $f$  for a limited set of discrete angles  $\theta \in \mathbb{S}^{n-1}$  and discrete points  $t \in \mathbb{R}$ , we evaluate  $I_\gamma^h(z)$  numerically to approximate  $f(z)$  for every sampling point  $z$  in the domain  $\Omega$ .

**Parallel implementation of the DSM.** From the definition of the index function in (2.16), we can see a very attractive feature of the proposed DSM that the evaluations of the index function at different sampling points are independent of each other. Hence, the DSM can be implemented in a highly parallel manner, which can improve its efficiency significantly for large-scale reconstructions.

**3. Verification of the index function.** In this section, we aim to verify that our proposed index function in (2.16) can recover the target function  $f$  accurately (see subsection 3.1 for the Sobolev scale  $\gamma \in ((n-1)/2, n/2)$  and subsection 3.3 for  $\gamma \in (0, (n-1)/2]$ ) and stably (see subsections 3.3 and 3.4). In particular, the verification for the latter case relies on the alternative characterization of the index function that will be presented in subsection 3.2. Moreover, the choice of the key parameter  $\alpha = n+1$  in the definition of the probing function (2.8) will also be explained in the same subsection. In subsection 3.4, we will demonstrate the relationship between the Sobolev scale  $\gamma$  in (2.5) and the variance of the index function under a particular noise model that provides crucial insight on the choice of  $\gamma$  during the reconstruction with noisy measurement data. In addition, the conclusion from subsection 3.4 implies the choice of  $\gamma \geq n/2$  is not preferable in real applications and hence we only consider the possibility of  $\gamma < n/2$  in the subsequent discussions.

**3.1. Convergence of the index function for  $(n-1)/2 < \gamma < n/2$ .** We will first focus on the case  $(n-1)/2 < \gamma < n/2$  and verify that the index function proposed in (2.16) can recover the target function  $f$  as  $h \rightarrow 0$ , separately for the smooth case  $f \in C^{0,1}(\Omega)$  and the nonsmooth case  $f \in L^\infty(\Omega)$ . The parameter  $h$  could be considered as the sampling interval in real applications.

**Lemma 3.1.** Let  $I_\gamma^h$  be the index function defined in (2.16).

(a) For any  $f \in C^{0,1}(\Omega)$  and  $z \in \Omega$ , it holds that

$$(3.1) \quad |I_\gamma^h(z) - f(z)| \leq h^{1 - \frac{2}{4+2\gamma-n}} (\|f\|_{C^{0,1}(\Omega)} + 2c_1(n, \gamma) \|f\|_{L^\infty(\Omega)}) + \mathcal{O}(h^{3+2\gamma-n})$$

for some positive constant  $c_1(n, \gamma)$  that depends only on  $n$  and  $\gamma$ . In particular, the exponent of the leading order term with respect to  $h$ , that is,  $1 - 2/(4 + 2\gamma - n)$ , is larger than  $1/3$  for all  $\gamma > (n - 1)/2$ .

(b) For any  $f \in L^\infty(\Omega)$ , it holds that

$$(3.2) \quad \|I_\gamma^h - f\|_{L^2(\Omega)} \leq h^{\frac{1}{2} - \frac{1}{4+2\gamma-n}} c_2(\Omega, \gamma) \|f\|_{L^\infty(\Omega)} + \mathcal{O}(h^{3+2\gamma-n})$$

for some positive constant  $c_2(\Omega, \gamma)$  that depends only on  $\Omega$  and  $\gamma$ . In particular, the exponent of the leading order term with respect to  $h$ , that is,  $1/2 - 1/(4 + 2\gamma - n)$ , is larger than  $1/6$  for all  $\gamma > (n - 1)/2$ .

*Proof.* (a) First, based on the inversion formula (2.4) and the self-adjointness of the fractional Laplacian which holds due to parts (b) and (c) of Lemma 2.1, we can write

$$(3.3) \quad \begin{aligned} \langle u_s, \eta_z^h \rangle_\gamma &= \int_{\mathbb{R}^n} u_s(x) (-\Delta)^\gamma \eta_z^h(x) dx = \int_{\mathbb{R}^n} (-\Delta)^{\gamma - \frac{n-1}{2}} f(x) \eta_z^h(x) dx \\ &= \int_{\mathbb{R}^n} f(x) (-\Delta)^{\gamma - \frac{n-1}{2}} \tilde{\eta}_z^h(x) dx + \int_{\mathbb{R}^n} (-\Delta)^{\gamma - \frac{n-1}{2}} f(x) [\eta_z^h(x) - \tilde{\eta}_z^h(x)] dx. \end{aligned}$$

For the second integration above, by definitions of  $\eta_z^h$  and  $\tilde{\eta}_z^h$  in (2.8) and (2.9), we have

$$(3.4) \quad \begin{aligned} \left| \int_{\mathbb{R}^n} (-\Delta)^{\gamma - \frac{n-1}{2}} f [\eta_z^h - \tilde{\eta}_z^h] dx \right| &\leq \|(-\Delta)^{\gamma - \frac{n-1}{2}} f\|_{L^\infty(\mathbb{R}^n)} \|\zeta_{n+1}^h - \tilde{\zeta}_{n+1}^h\|_{L^1(\mathbb{R}^n)} \\ &\leq \|(-\Delta)^{\gamma - \frac{n-1}{2}} f\|_{L^\infty(\mathbb{R}^n)} h, \end{aligned}$$

where the boundness of the term  $\|(-\Delta)^{\gamma - \frac{1}{2}} f\|_{L^\infty(\mathbb{R}^n)}$  follows from  $f \in C^{0,1}(\mathbb{R}^n)$  and the estimate (2.14).

Moreover, by substituting  $\tilde{\eta}_0^1(\frac{x}{h}) = h^{n+1} \tilde{\eta}_0^h(x)$  which comes from (2.7) and (2.9) into the definition of the fractional Laplacian operator, we further have the following rescaling property:

$$(3.5) \quad (-\Delta)^{\gamma - \frac{n-1}{2}} (\tilde{\eta}_0^h)(x) = h^{n+1+2\gamma} ((-\Delta)^{\gamma - \frac{n-1}{2}} \tilde{\eta}_0^1) \left( \frac{x}{h} \right).$$

For simplicity, we write  $\beta = \gamma - \frac{n-1}{2}$ . By part (c) of Lemma 2.1 that  $(-\Delta)^\beta \tilde{\eta}_0^1 \in L^2(\mathbb{R}^n) \subset L^1(\mathbb{R}^n)$ , we can define a family of approximations to the identity for all  $f \in C^{0,1}(\Omega)$ :

$$(3.6) \quad \tau_\beta^h(x) = \frac{h^{-n} (-\Delta)^\beta \tilde{\eta}_0^1(\frac{x}{h})}{\|(-\Delta)^\beta \tilde{\eta}_0^1\|_{L^1(\mathbb{R}^n)}} = h^{1+2\gamma} \frac{(-\Delta)^\beta (\tilde{\eta}_0^h)(x)}{\|(-\Delta)^\beta \tilde{\eta}_0^1\|_{L^1(\mathbb{R}^n)}}.$$

For any  $\nu > 0$ , by definition, the integration of  $\tau_\beta^h$  satisfies a rescaling property

$$\int_{B(0, h^\nu)} \tau_\beta^h(y) dy = \int_{B(0, h^{\nu-1})} \tau_\beta^1(y) dy.$$

Using the above defined family of the approximations to the identity, we can derive

$$\begin{aligned}
 \left| \int_{\mathbb{R}^n} f(y) \tau_\beta^h(z-y) dy - f(z) \right| &\leq \left| h^{2\nu} \|f\|_{C^{0,1}(\Omega)} \int_{B(0, h^{\nu-1})} \tau_\beta^1(y) dy \right. \\
 &\quad \left. + 2 \|f\|_{L^\infty} \int_{\mathbb{R}^n \setminus B(0, h^{\nu-1})} \tau_\beta^1(y) dy \right| \\
 (3.7) \qquad \qquad \qquad &\leq h^{2\nu} \|f\|_{C^{0,1}(\Omega)} + 2c_1(n, \gamma) \|f\|_{L^\infty(\Omega)} h^{(1-\nu)(1+2\beta)},
 \end{aligned}$$

where the positive constant  $c(n, \gamma)$  only depends on the dimension and  $\gamma$ . The last inequality above is from our proof in Lemma 2.1 following (2.15) which implies  $(-\Delta)^\beta \tau_\beta^h \leq c'(n, \gamma) |x|^{-\alpha-2\beta}$  for  $x > 2h$  and  $c'(n, \gamma)$  that is independent of  $h$ .

Combining (3.3) and (3.7), we can conclude that for any sampling point  $z \in \Omega$  and  $\nu > 0$ ,

$$\begin{aligned}
 &\left| h^{1+2\gamma} \langle u_s, \eta_z^h \rangle_\gamma - \|(-\Delta)^{\gamma-\frac{n-1}{2}} \tilde{\eta}_0^1\|_{L^1(\mathbb{R}^n)} f(z) \right| \\
 &\leq \|(-\Delta)^{\gamma-\frac{n-1}{2}} \tilde{\eta}_0^1\|_{L^1(\mathbb{R}^n)} (h^{2\nu} \|f\|_{C^{0,1}(\Omega)} + 2h^{(1-\nu)(1+2\beta)} \|f\|_{L^\infty(\Omega)} c_1(n, \gamma)) \\
 (3.8) \qquad \qquad \qquad &+ h^{2+2\gamma} \|(-\Delta)^{\gamma-\frac{n-1}{2}} f\|_{L^\infty(\mathbb{R}^n)}.
 \end{aligned}$$

We pick  $\nu$  such that  $2\nu = (1-\nu)(1+2\beta)$ , i.e.,  $\nu = 1/2 - 1/(3+2\beta)$  that is the optimal order of  $h$ .

Next, replacing  $u_s$  and  $f$  in (3.8) by  $R^*R(\mathbb{1}_\Omega)$  and  $\mathbb{1}_\Omega$ , we derive for  $z \in \Omega$  and  $n(z)$  from (2.16),

$$\begin{aligned}
 \left| h^{1+2\gamma} n(z) - \|(-\Delta)^{\gamma-\frac{n-1}{2}} \tilde{\eta}_0^1\|_{L^1(\mathbb{R}^n)} \right| &= \left| h^{1+2\gamma} \langle d_n R^*R(\mathbb{1}_\Omega), \eta_z^h \rangle_\gamma - \|(-\Delta)^{\gamma-\frac{n-1}{2}} \tilde{\eta}_0^1\|_{L^1(\mathbb{R}^n)} \right| \\
 &\leq 2 \|(-\Delta)^{\gamma-\frac{n-1}{2}} \tilde{\eta}_0^1\|_{L^1(\mathbb{R}^n)} h^{1+2\beta}.
 \end{aligned}$$

With the above two estimates and the definition (2.16) of  $I_\gamma^h$ , we readily derive

$$\begin{aligned}
 (3.9) \quad \left| I_\gamma^h(z) - \frac{h^{1+2\gamma} \langle u_s, \eta_z^h \rangle_\gamma}{\|(-\Delta)^{\gamma-\frac{n-1}{2}} \tilde{\eta}_0^1\|_{L^1(\mathbb{R}^n)}} \right| &= \frac{\langle u_s, \eta_z^h \rangle_\gamma}{n(z)} \frac{\|(-\Delta)^{\gamma-\frac{n-1}{2}} \tilde{\eta}_0^1\|_{L^1(\mathbb{R}^n)} - h^{1+2\gamma} n(z)}{\|(-\Delta)^{\gamma-\frac{n-1}{2}} \tilde{\eta}_0^1\|_{L^1(\mathbb{R}^n)}} \\
 &\leq 2 \|f\|_{L^\infty(\Omega)} h^{1+2\beta}.
 \end{aligned}$$

Combining (3.8) and (3.9), we conclude that

$$\begin{aligned}
 |I_\gamma^h(z) - f(z)| &\leq h^{1-\frac{2}{3+2\beta}} (\|f\|_{C^{0,1}(\Omega)} + 2c_1(n, \gamma) \|f\|_{L^\infty(\Omega)}) + \frac{h^{2+2\gamma} \|(-\Delta)^{\gamma-\frac{1}{2}} f\|_{L^\infty(\mathbb{R}^n)}}{\|(-\Delta)^{\gamma-\frac{n-1}{2}} \tilde{\eta}_0^1\|_{L^1(\mathbb{R}^n)}} \\
 (3.10) \quad &+ 2 \|f\|_{L^\infty(\Omega)} h^{1+2\beta} = h^{1-\frac{2}{4+2\gamma-n}} (\|f\|_{C^{0,1}(\Omega)} + 2c_1(n, \gamma) \|f\|_{L^\infty(\Omega)}) + \mathcal{O}(h^{3+2\gamma-n}),
 \end{aligned}$$

which is the desired result for the first part of the lemma.

(b) For the sake of notation, we write the output reconstructed from the target function  $f$  by index  $I_\gamma^h$  as  $I_\gamma^{h,f}$ . We can first observe that  $\|I_\gamma^{h,f}\|_{L^2(\Omega)} \leq c'(\Omega, \gamma) \delta$  with  $c'$  independent of  $h$  if  $\|f\|_{L^2(\Omega)} \leq \delta$ , with an application of the Fubini's theorem.

For a given  $f \in L^\infty(\Omega)$ , we recall that  $f$  can be approximated arbitrarily accurately by a sum of characteristic function in the  $L^2$  sense. Hence, without loss of generality, we assume  $f = M\mathbb{1}_U$ , a scaled characteristic function over a compact set  $U \subset \Omega$  ( $M > 0$ ). Now we consider a family of smooth modifiers  $\{\rho^\delta\}_{\delta>0}$  (with  $c$  chosen such that  $\int_{\mathbb{R}^n} \rho(x) = 1$ ):

$$\rho(x) := \begin{cases} c \exp(-\frac{1}{1-|x|^2}) & \text{for } |x| < 1, \\ 0 & \text{otherwise;} \end{cases} \quad \rho^\delta(x) := \frac{1}{\delta^n} \rho\left(\frac{x}{\delta}\right),$$

Then we have  $f * \rho^\delta \in C^\infty(\Omega)$ , and  $\|f - f * \rho^\delta\|_{L^2(\Omega)} \leq c_3(\Omega)M\delta$  with  $c_3$  independent of  $h$ , therefore

$$(3.11) \quad \|I_\gamma^{h,f} - I_\gamma^{h,f*\rho^\delta}\|_{L^2(\Omega)} \leq c_3(\Omega)M\delta.$$

To compare  $f * \rho^\delta$  and  $I_\gamma^{h,f*\rho^\delta}$ , we need to estimate  $\|f * \rho^\delta\|_{C^{0,1}(\Omega)}$  from (3.10). We can compute

$$(3.12) \quad \frac{d}{dx_i} f * \rho^\delta(x) = \int_{\mathbb{R}^n} f(t) \frac{d}{dx_i} \rho^\delta(x-t) dt \leq \frac{M}{\delta} \int_{\mathbb{R}^n} \frac{\partial}{\partial x_i} \rho(x-t) dt,$$

which implies  $\|f * \rho^\delta\|_{C^{0,1}(\Omega)} \leq \delta^{-1}c_4(n, \gamma)$ . By (3.10) and (3.12), then we further derive

$$(3.13) \quad \|f * \rho^\delta - I_\gamma^{h,f*\rho^\delta}\|_{L^2(\Omega)} \leq c_4(\Omega, \gamma)Mh^{\frac{1}{2}-\frac{1}{4+2\gamma-n}} + \mathcal{O}(h^{3+2\gamma-n}).$$

Combining all the above estimates and choosing  $\delta = h^{\frac{1}{2}-\frac{1}{3+2\beta}}$ , we come to the desired estimate:

$$\begin{aligned} \|I_\gamma^{h,f} - f\|_{L^2(\Omega)} &\leq \|I_\gamma^{h,f} - I_\gamma^{h,f*\rho^\delta}\|_{L^2(\Omega)} + \|I_\gamma^{h,f*\rho^\delta} - f * \rho^\delta\|_{L^2(\Omega)} + \|f * \rho^\delta - f\|_{L^2(\Omega)} \\ &\leq h^{\frac{1}{2}-\frac{1}{4+2\gamma-n}} c_2(\Omega, \gamma) \|f\|_{L^\infty(\Omega)} + \mathcal{O}(h^{3+2\gamma-n}). \end{aligned} \quad \blacksquare$$

We see from Lemma 3.1 that the convergence rates are different for smooth and non-smooth  $f$ . However, we have observed from our numerical experience that the DSM performs quite similarly and robustly for both smooth and nonsmooth images. Hence, we shall mainly examine the DSM for nonsmooth target functions in section 6, as most real images are usually nonsmooth and may have sharp edges.

We shall make the justification of the index function for the case of the Sobolev scale  $\gamma \leq (n-1)/2$  in section 3.3. Before that, we next present an alternative characterization of the index function which explains the choice of  $\alpha$  in (2.8). This alternative characterization will be also essential to our subsequent justification of the index function for  $\gamma \leq (n-1)/2$ .

In the remainder of this section, with the help of the remark that we mentioned after (2.4), we further assume that the target function  $f$  is a smooth function.

**3.2. Alternative characterization of the index function.** In this subsection, we present an alternative characterization of the index function defined in (2.16) for all possible choices of  $\gamma \in (0, \frac{n}{2})$ . The characterization is mainly to obtain a dominating term in the index function with respect to the small parameter  $h$  involved in the probing function (2.7). More specifically, we shall show that the index function at the sampling point  $z$  approximately equals the average of  $(-\Delta)^\gamma u_s$  at the neighborhood of  $z$ . This characterization will be used in two ways:

- We shall justify that the preferable choice of the key parameter  $\alpha \in \mathbb{R}$  involved in the probing function is  $\alpha = n + 1$ , as we suggested in (2.8). To do so, we will estimate and investigate the dominating term of the index function when the probing function (2.8) is used or replaced by other functions  $\zeta_\alpha^h$  with  $\alpha \neq n + 1$ .
- The dominating term in the index function will provide an essential tool to help us justify that the proposed DSM can approximately recover the target function  $f$  when  $\gamma \in (0, (n - 1)/2]$  in subsection 3.3.

**Lemma 3.2.** For  $\alpha = n + 1$ , the duality product defined in (2.5) between the measurement data  $u_s$  and the probing function  $\eta_z^h$  can be written as

$$(3.14) \quad \langle u_s, \eta_z^h \rangle_\gamma = h^{-1} \int_{B(z,h)} u_s dx + \mathcal{O}(1).$$

*Proof.* Let us first assume  $\alpha = n + 1$ , which is the one used in the definition (2.8). To obtain a dominating term of the numerator of the index function, we rewrite it, by using direct addition and subtraction, as

$$(3.15) \quad \begin{aligned} \langle u_s, \eta_z^h \rangle_\gamma &= \underbrace{\int_{\mathbb{R}^n} (-\Delta)^\gamma u_s [\eta_z^h - \tilde{\eta}_z^h] dx}_{\phi_1(z)} - \frac{1}{n-1} \underbrace{\int_{\mathbb{R}^n} (-\Delta)^{\gamma+1} u_s \left[ \tilde{\zeta}_{n-1}^h(x-z) - \frac{1}{|x-z|^{n-1}} \right] dx}_{\phi_2(z)} \\ &- \frac{1}{n-1} \underbrace{\int_{\mathbb{R}^n} (-\Delta)^{\gamma+1} u_s \frac{1}{|x-z|^{n-1}} dx}_{\phi_3(z)} + \underbrace{\int_{\mathbb{R}^n} \left[ (-\Delta)^\gamma u_s \tilde{\eta}_z^h + \frac{1}{n-1} (-\Delta)^{\gamma+1} u_s \tilde{\zeta}_{n-1}^h(x-z) \right] dx}_{\phi_4(z)}, \end{aligned}$$

where  $\tilde{\zeta}_{n-1}^h$  is defined in (2.7) and the derivation of the constant  $1/(n-1)$  in (3.15) will be introduced in the analysis of  $\phi_4(z)$ .

We now investigate the properties of the terms  $\phi_i(z)$  ( $1 \leq i \leq 4$ ) one by one. For  $\phi_1(z)$ , the estimate is identical with (3.4), so we have

$$(3.16) \quad |\phi_1(z)| \leq \|(-\Delta)^{\gamma-\frac{1}{2}} f\|_{L^\infty(\mathbb{R}^n)} h.$$

Next, for  $\phi_2(z)$ , recalling the definition of  $\zeta_{n-1}^h$  in (2.7), we notice the integrand vanishes if  $|x-z| > h$ , which leads to

$$(3.17) \quad |\phi_2(z)| = \left| \int_{|x-z| \leq h} (-\Delta)^{\gamma+1} u_s \left[ \frac{1}{|x-z|^{n-1}} - \frac{1}{h^{n-1}} \right] dx \right| \leq 4\pi \|(-\Delta)^{\gamma+\frac{1}{2}} f\|_{L^\infty(\Omega)} h.$$

To consider the term  $\phi_3(z)$ , we make use of a convenient representation of a smooth function  $g$  from harmonic analysis (e.g., [24]):

$$(-\Delta)^{-\gamma} g(z) = c_{n,-\gamma} \int_{\mathbb{R}^n} \frac{g(x)}{|x-z|^{n-1}} dx \quad \text{with} \quad c_{n,-\gamma} = \frac{\Gamma(\frac{n}{2} - \gamma)}{4^\gamma \pi^{\frac{n}{2}} \Gamma(\gamma)}.$$

Using this property, taking  $g = (-\Delta)^{\gamma+1}u_s$  and  $\gamma = 1/2$ , we have

$$(3.18) \quad \phi_3(z) = \frac{1}{c(n, -\frac{1}{2})}(-\Delta)^{-\frac{1}{2}}((-\Delta)^{\gamma+1}u_s(z)) = \frac{1}{c(n, -\frac{1}{2})}(-\Delta)^{\gamma+\frac{1}{2}}u_s(z).$$

To summarize, we notice that the orders of  $\phi_1(z)$  and  $\phi_2(z)$  are  $\mathcal{O}(h)$ , and the magnitude of  $\phi_3(z)$  is independent of the choice of  $h$ .

Finally, we come to analyze  $\phi_4(z)$ . Since  $(-\Delta)\tilde{\zeta}_{n-1}^h(x) = -(n-1)\tilde{\zeta}_{n+1}^h(x)$  for  $|x| > h$ , the Green's identity leads to

$$(3.19) \quad \begin{aligned} \phi_4(z) &= \int_{\mathbb{R}^n} \left[ (-\Delta)^\gamma u_s \tilde{\zeta}_{n+1}^h(x) + \frac{1}{n-1}(-\Delta)^{\gamma+1}u_s \tilde{\zeta}_{n-1}^h(x-z) \right] dx \\ &= \int_{\partial B(z,h)} (-\Delta)^\gamma u_s \frac{\partial}{\partial n^-} \frac{1}{|x-z|^{n-1}} dx_s + \frac{1}{h^{n+1}} \int_{B(z,h)} (-\Delta)^\gamma u_s dx \\ &= \frac{1}{h^n} \int_{\partial B(z,h)} (-\Delta)^\gamma u_s dx_s + \frac{1}{h^{n+1}} \int_{B(z,h)} (-\Delta)^\gamma u_s dx, \end{aligned}$$

where  $n^-$  denotes the normal vector pointing toward  $z$ . The simplification of the integration on  $\partial B(z, h)$  comes from the definition of  $\tilde{\zeta}_{n-1}^h$ , since it is a constant inside  $B(z, h)$ .

We can observe from (3.19) that the order of  $\phi_4(z)$  is  $\mathcal{O}(h^{-1})$ , which is larger than the orders  $\mathcal{O}(1)$  of  $\phi_i(z)$  ( $1 \leq i \leq 3$ ). Hence we can now conclude that the dominating term in the duality product  $\langle u_s, \eta_z^h \rangle_\gamma$  is  $\phi_4(z)$ , which is the desired result in (3.14). ■

From the above lemma and especially the final approximation in (3.14),  $\langle u_s, \eta_z^h \rangle_\gamma$  can be readily seen as a good approximation of the average of  $(-\Delta)^\gamma u_s$  in a close neighborhood of the sampling point  $z$ . This fact will be used in section 3.3.

We are now ready to justify our choice of  $\alpha = n + 1$  in the definition of the probing function in (2.8). First, the choice of  $\alpha \leq n$  is not applicable as  $\zeta_\alpha^h \notin L^1(\mathbb{R}^n)$ . In this case, the index function (2.16) which involves integration in  $\mathbb{R}^n$  might not always be well defined and we can not ensure its accuracy and stability of reconstruction.

Second, for the choice of  $\alpha > n + 1$ , there are two reasons that this option is not preferable. The first one is that the  $L^\infty$ -norm of the auxiliary function  $\zeta_\alpha^h$  in (2.7) is of order  $h^{-\alpha}$ . Hence, a larger choice of  $\alpha > n + 1$  may lead to an issue of numerical instability. Let us discuss a special case of  $\alpha > n + 1$  below, i.e.,  $\alpha = n + 3$ , and we will conclude that the dominating term in the duality product between  $u_s$  and  $\zeta_{n+3}^h$  is the same as the dominating term in the duality product between  $u_s$  and  $\zeta_{n+1}^h$  (the probing function we employed in DSM). We will compare the numerical reconstructions (see Example 1, section 6), with  $\alpha$  being  $n + 1$ ,  $n + 2$ , and  $n + 3$ , to justify the choice of  $\alpha = n + 1$  in our DSM.

Let us now consider the case  $\alpha = n + 3$ , that is, the probing function (2.8) used in the index function (2.16) is replaced by  $\zeta_{n+3}^h$ . We first observe that  $(-\Delta)^2 \tilde{\zeta}_{n-1}^h(x) = 1/e(n)\tilde{\zeta}_{n+3}^h(x)$  for  $x > h$  with  $e(n) = 1/3(n^2 - 1)$ . We rewrite the duality product between  $u_s$  and  $\zeta_{n+3}^h$  like in (3.15):

$$\begin{aligned} \langle u_s, \zeta_{n+3}^h(x-z) \rangle_\gamma &= \underbrace{\int_{\mathbb{R}^n} (-\Delta)^\gamma u_s [\zeta_{n+3}^h(x-z) - \tilde{\zeta}_{n+3}^h(x-z)] dx}_{\tilde{\phi}_1(z)} - e(n) \underbrace{\int_{\mathbb{R}^n} (-\Delta)^{\gamma+2} u_s [\tilde{\zeta}_{n-1}^h(x-z) - |x-z|^{-n+1}] dx}_{\tilde{\phi}_2(z)} \\ &- e(n) \underbrace{\int_{\mathbb{R}^n} (-\Delta)^{\gamma+2} u_s |x-z|^{-n+1} dx}_{\tilde{\phi}_3(z)} + \underbrace{\int_{\mathbb{R}^n} [(-\Delta)^\gamma u_s \tilde{\zeta}_{n-1}^h(x-z) + e(n)(-\Delta)^{\gamma+2} u_s \tilde{\zeta}_{n+3}^h(x-z)] dx}_{\tilde{\phi}_4(z)}. \end{aligned}$$

The estimates for  $\tilde{\phi}_i(z)$  ( $1 \leq i \leq 3$ ) are basically the same as the above estimates for  $\phi_i(z)$  ( $i \leq 1 \leq 3$ ), expect the minor differences in replacing the order of the fractional Laplacian from  $\gamma + 1/2$  to  $\gamma + 3/2$  in the right-hand side of (3.17) and (3.18). For  $\tilde{\phi}_4(z)$ , we can apply the Green's identity twice to derive

$$(3.20) \quad \tilde{\phi}_4(z) = \frac{c_5(n, \gamma)}{h^{n+1}} \int_{\partial B(z, h)} (-\Delta)^\gamma u_s dx_s + \frac{1}{h^{n+2}} \int_{B(z, h)} (-\Delta)^\gamma u_s dx + \mathcal{O}(h^{-1}),$$

where  $c_5(n, \gamma)$  is a positive constant independent of  $z$  and  $h$ .  $\tilde{\phi}_4(z)$  now still represents the average of  $(-\Delta)^\gamma u_s$  over the neighborhood of  $z$ . We can conclude that the dominating terms of the index function with  $\alpha = n + 1$  and  $\alpha = n + 3$  are approximately the same. Although the order of  $\tilde{\phi}_4(z)$  in (3.20) with  $\alpha = n + 3$  is higher than  $\phi_4(z)$  in (3.19) with  $\alpha = n + 1$ , we point out that the difference in order has a minor influence on the accuracy of the reconstruction as the magnitude of  $\phi_i(z)$  and  $\tilde{\phi}_i(z)$ ,  $i = 1, 2, 3$ , are much smaller than both of  $\phi_4(z)$  and  $\tilde{\phi}_4(z)$ . Moreover, as we are particularly interested in reconstruction with noisy and inadequate measurement data, it is preferable to choose a probing function that is smoother and has a smaller  $L^\infty$ -norm.

With the above considerations and Lemma 3.2, in order to maintain the appropriate regularity of the probing function as well as to minimize numerical instability, we shall, from now on, only consider a choice of  $\alpha$  in the range  $\alpha \in (n, n + 1]$ . From numerical experiments, we do not observe much difference in the quality of numerical reconstruction for any choice of  $\alpha \in (n, n + 1]$ , and therefore for simplicity, we always choose the probing function (2.8) with  $\alpha = n + 1$  instead of some other probing functions  $\zeta_\alpha^h$  with  $\alpha \neq n + 1$ .

**3.3. Verification of the index function for  $0 < \gamma \leq (n - 1)/2$  and the frequency domain representation of the probing function.** In this section, we shall first verify that our proposed index function  $I_\gamma^h$  approximately recovers the target function  $f$  when  $0 < \gamma \leq (n - 1)/2$ , and then present a frequency domain representation of the function  $\tilde{\eta}_z^h$ . This representation reveals the fact that the application of the probing function can be regarded as applying a low pass filter on the measurement data, which helps us better understand the importance and necessity of computing the duality product between the measurement data and the chosen probing function  $\eta_z^h$ .

To verify that the index function can properly recover the target function  $f$ , we first recall the critical motivation for direct sampling type methods in (2.3), that  $u_s = d_n R^* R f$  can be represented by the convolution of  $f$  and a fast decaying kernel function  $G_x(y) = 1/|x - y|$ . It can be observed that  $G_x(y)$  is very large when  $x \approx y$  and is relatively small otherwise. Hence, if we are given noisy or inadequate measurement data,  $u_s$  is already an approximation to the target function  $f$ . Furthermore, considering the reconstruction by the proposed DSM

with  $\gamma \leq (n - 1)/2$ , we next show that our method can improve the approximation to the target function  $f$  compared with the approximation provided by  $u_s$  without applying any pseudodifferential operator on the noisy measurement data.

First, by the singular integral representation of negative order fractional Laplacians, we have

$$(3.21) \quad (-\Delta)^\gamma u_s(x) = (-\Delta)^{\gamma - \frac{n-1}{2}} f(x) = \frac{\Gamma((n + 1)/4 + \gamma/2)}{2^{(n+1)/2 - \gamma} \pi^{n/2} \Gamma((n - 1)/4 - \gamma/2)} \int_{\Omega} \frac{f(y)}{|y - x|^{\frac{n+1}{2} + \gamma}} dy.$$

We observe that the integration in the right-hand side is simply the convolution of  $f$  and  $1/|x|^{(n+1)/2 + \gamma}$ . As  $\gamma$  becomes larger, the convolution kernel  $1/|x|^{(n+1)/2 + \gamma}$  becomes more concentrated at the origin, hence  $(-\Delta)^\gamma u_s$  provides a better approximation to  $f(x)$ . In particular, as  $\gamma \rightarrow (n - 1)/2$ ,  $(-\Delta)^\gamma u_s$  also converges to the target function  $f(x)$  up to a normalization constant that follows from the inversion formula (2.4).

Now we recall the alternative characterization of the index function that we obtained through the discussion following (3.19) in section 3.2. The dominating term of the duality product  $\langle u_s, \eta_z^h \rangle_\gamma$  is the average of  $(-\Delta)^\gamma u_s$  at the neighborhood of the sampling point  $z$ . Moreover, with the same reason, the denominator of the index function which equals to  $\langle d_n R^* R(\mathbb{1}_\Omega), \eta_z^h \rangle_\gamma$  also approximately equals to a constant in  $\Omega$ . Hence, this justifies that our index function can approximately recover  $f$  due to the approximation property of  $(-\Delta)^\gamma u_s$  and the alternative characterization of the index function.

We shall remark that, although computing  $(-\Delta)^{\frac{n-1}{2}} u_s$  recovers  $f$  exactly in the noise-free case, the choice of  $\gamma = (n - 1)/2$  is not preferable in applications that we mentioned in the introduction due to numerical instability. This theoretical prediction will also be justified in section 3.4 and Example 1 of section 6.

In the remaining part of this subsection, we would like to investigate the frequency domain representation of the probing function. The main motivation for this part is that the discussion following (3.21) implies that the reconstruction solely with  $(-\Delta)^\gamma u_s$  is already an approximation to the target function  $f$ . Therefore, it is necessary for us to justify that the introduction of the duality product and the probing function in the new DSM are essential in recovering the target function  $f$  more stably. First, by the definitions (2.5) and (2.16), the duality product allows us to avoid applying a pseudodifferential operator directly on the noisy measurement data  $u_s$ . Moreover, we will now show that our choice of the probing function induces a low pass filter in the frequency domain. For this reason, it helps improve the quality of reconstruction with noisy measurement data. To justify the low pass filtering property of the probing function, we consider the numerator of the index function in the frequency domain which yields

$$(3.22) \quad \langle u_s, \eta_z^h \rangle_\gamma = \int_{\mathbb{R}^n} (-\Delta)^\gamma u_s \tilde{\eta}_z^h dx + \int_{\mathbb{R}^n} (-\Delta)^\gamma u_s [\eta_z^h - \tilde{\eta}_z^h] dx = \mathcal{F}^{-1} \left\{ \mathcal{F}(\tilde{\eta}_0^h) \mathcal{F}((-\Delta)^\gamma u_s) \right\} + \phi_1(z),$$

where  $\mathcal{F}^{-1}$  denotes the inverse Fourier transform and  $\phi_1(z)$  is defined in (3.15) which is of the order  $\mathcal{O}(h)$  by (3.16). The representation of the duality product in (3.22) implies that the

reconstruction by the proposed DSM can be regarded as applying the filtering function induced by  $\tilde{\eta}_0^h$  on  $(-\Delta)^\gamma u_s$ . Therefore, we now investigate the Fourier transform of  $\tilde{\eta}_0^h$  explicitly to show the following.

**Lemma 3.3.** Denoting  $\lambda = 2\pi h|\omega|$ , the Fourier transform of  $\tilde{\eta}_0^h$  defined in (2.9) can be written as

$$\mathcal{F}(\tilde{\eta}_0^h)(\omega) = \begin{cases} \frac{1}{h} \frac{J_1(\lambda)}{\lambda} + \frac{\lambda}{h} \left[ \left( \frac{\lambda^2+1}{\lambda} - \frac{\pi\lambda}{2} \mathbf{H}_1(\lambda) \right) J_0(\lambda) - \left( 1 - \frac{\pi\lambda}{2} \mathbf{H}_0(\lambda) \right) J_1(\lambda) - 1 \right], & n = 2, \\ \frac{4\pi}{h} \left[ \frac{\sin(\lambda) - \lambda \cos(\lambda)}{\lambda^3} + \lambda \left( \frac{-\pi + 2\text{Si}(\lambda)}{4} + \frac{\sin(\lambda)}{2\lambda^2} + \frac{\cos(\lambda)}{2\lambda} \right) \right], & n = 3. \end{cases}$$

*Proof.* For  $n = 2$ , we use the Fourier Bessel transform:

$$\int_{\mathbb{R}^2} \tilde{\eta}_0^h(|x|) e^{-i2\pi x \cdot \omega} dx = \int_{\mathbb{R}} \tilde{\eta}_0^h(r) J_0(2\pi|\omega|r) r dr,$$

where  $J_\nu$  is the Bessel function of the first kind of order  $\nu$ . This can be simplified to a one-dimensional integration involving the Bessel function:

(3.23)

$$\begin{aligned} \mathcal{F}(\tilde{\eta}_0^h)(\omega) &= \int_0^h \frac{J_0(2\pi|\omega|r)r}{h^3} dr + \int_h^\infty \frac{J_0(2\pi|\omega|r)}{r^2} dr \\ &= \frac{1}{4\pi^2|\omega|^2 h^3} \int_0^{2\pi|\omega|h} J_0(t) t dt + 2\pi|\omega| \left[ \int_0^\infty \frac{J_0(t) - 1}{t^2} dt + \int_{2\pi|\omega|h}^\infty \frac{1}{t^2} dt + \int_0^{2\pi|\omega|h} \frac{1 - J_0(t)}{t^2} dt \right]. \end{aligned}$$

Moreover, we notice the following integrals regarding Bessel functions of the first kind in [1]:

$$(3.24) \quad \begin{aligned} \int_0^x J_0(t) t dt &= x J_1(x), \quad \int_0^\infty \frac{1 - J_0(t)}{t^2} dt = 1, \\ \int_0^x \frac{1 - J_0(t)}{t^2} dt &= -\frac{1}{x} - \left[ 1 - \frac{\pi x}{2} \mathbf{H}_0(x) \right] J_1(x) + \left[ \frac{x^2 + 1}{x} - \frac{\pi x}{2} \mathbf{H}_1(x) \right] J_0(x), \end{aligned}$$

where  $\mathbf{H}_\nu$  is the Struve function of order  $\nu$ . Combining the above computations, we conclude that

$$\mathcal{F}(\tilde{\eta}_0^h)(\omega) = \frac{1}{h} \frac{J_1(\lambda)}{\lambda} + \frac{\lambda}{h} \left[ \left( \frac{\lambda^2+1}{\lambda} - \frac{\pi\lambda}{2} \mathbf{H}_1(\lambda) \right) J_0(\lambda) - \left( 1 - \frac{\pi\lambda}{2} \mathbf{H}_0(\lambda) \right) J_1(\lambda) - 1 \right], \quad \lambda = 2\pi|\omega|h.$$

For the case  $n = 3$ , we first consider the identity regarding the Fourier transform of a radial function in  $\mathbb{R}^3$ :

$$\int_{\mathbb{R}^3} f(|x|) e^{-2\pi i x \cdot \omega} dx = 2\pi \int_0^\infty \int_0^\pi f(r) e^{-2\pi i r \cos \theta |\omega|} r^2 d(-\cos \theta) dr = \frac{2}{|\omega|} \int_0^\infty f(r) r \sin(2\pi r |\omega|) dr;$$

then we can derive (with Si being the sine integral function and  $\lambda = 2\pi h|\omega|$ )

$$\begin{aligned}
 \mathcal{F}(\tilde{\eta}_0^h)(\omega) &= \frac{2}{|\omega|} \left[ \int_0^h \frac{r}{h^4} \sin(2\pi r|\omega|) dr + \int_h^\infty \frac{1}{r^3} \sin(2\pi r|\omega|) dr \right] \\
 &= \frac{2}{|\omega|} \left[ \frac{1}{h^4 4\pi^2 |\omega|^2} \int_0^{2\pi|\omega|h} t \sin(t) dt + 4\pi^2 |\omega|^2 \int_{2\pi|\omega|h}^\infty \frac{\sin(t)}{t^3} dt \right] \\
 &= \frac{4\pi}{h} \left[ \frac{\sin(\lambda) - \lambda \cos(\lambda)}{\lambda^3} + \lambda \left( \frac{-\pi + 2\text{Si}(\lambda)}{4} + \frac{\sin(\lambda)}{2\lambda^2} + \frac{\cos(\lambda)}{2\lambda} \right) \right]. \quad \blacksquare
 \end{aligned}$$

We know  $\mathcal{F}(\tilde{\eta}_0^h)(\omega) \in \mathbb{R}$  from Lemma 3.3, hence we now draw the values of the Fourier transform of  $\tilde{\eta}_0^h$  in  $\mathbb{R}^2$  (left) and  $\mathbb{R}^3$  (right), respectively, with respect to the norm of frequency domain variable, i.e.,  $|\omega|$  for a fixed  $h$  ( $h = 0.1$ ); see Figure 1. In particular, the value of  $\mathcal{F}(\tilde{\eta}_0^h)(\omega)$  depends only on  $\omega$ . Supposing the data is band-limited to  $1/(2h)$ , we observe that the frequency domain representation of  $\tilde{\eta}_0^h$  decays smoothly to 0 as  $|\omega|$  becomes larger. Hence, the probing function can be approximately viewed as a low pass filter since it cuts off the high frequency components and smoothes the low frequency component of the measurement data in both  $\mathbb{R}^2$  and  $\mathbb{R}^3$ .

To conclude, the crucial family of probing functions defined in (2.8) for the new DSM allows our reconstruction to be very stable under highly noisy measurement data since the application of the probing function can be regarded as applying a low pass filter on the measurement data as illustrated in Figure 1.

**3.4. Relationship between the Sobolev scale and the variance of the index function.**

In this subsection, we consider a particular noise model from [21] that approximates the measurement process to showcase some close relationship between the Sobolev scale  $\gamma$  in the duality product (2.5) and the variance of the index function for  $\gamma \in (0, 1)$ . We only consider the case  $\gamma < 1$  since the  $L^2$ -norm of  $(-\Delta)^\gamma \tilde{\eta}_z^h$  is bounded for  $\gamma < 1$  by part (c) of Lemma 2.1 and the boundedness of the  $L^2$ -norm is essential in our following discussion.

Suppose the collected data is polluted by a stationary zero-mean additive Gaussian noise, and the noise distributions are independent of each other for projections on different hyper-planes, namely, the noisy measurement takes the form

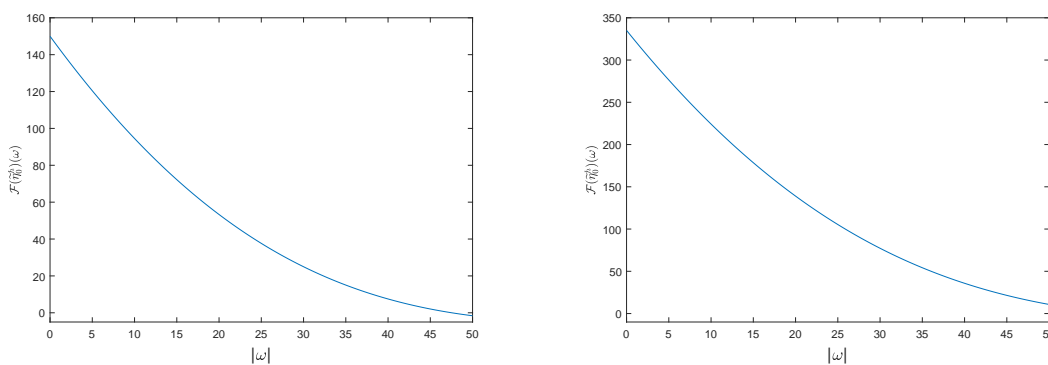


**Figure 1.** Frequency domain representation of  $\tilde{\eta}_0^h$  (cf. (2.7)) in  $\mathbb{R}^2$  (left) and  $\mathbb{R}^3$  (right), with the data being band-limited to  $1/(2h)$  ( $h = 0.1$ ). The horizontal and vertical axes are the norm of  $|\omega|$  and the value of the Fourier transform of  $\tilde{\eta}_0^h$ , respectively.

(3.25)

$$Rf(\theta, t) = Rf_e(\theta, t) + n(\theta, t), n(\theta, t) \sim N(0, \sigma_0^2), \mathbb{E}[n(\theta_1, t_1)n(\theta_2, t_2)] = \sigma_0^2\delta(\theta_1 - \theta_2)\delta(t_1 - t_2),$$

where  $\mathbb{E}$  represents the expectation operator,  $N(\mu, \sigma^2)$  stands for the normal distribution with mean  $\mu$  and standard deviation  $\sigma$ , and the subscript  $e$  denotes the exact value.

**Lemma 3.4.** *Under the assumption (3.25) on the measurement data, the variance of reconstruction, defined by  $\sigma_\gamma^2(z) = \mathbb{E}[(I_\gamma^h(z))^2] - \mathbb{E}[I_\gamma^h(z)]^2$ , satisfies*

$$(3.26) \quad [n(z)\sigma_\gamma(z)]^2 = \sigma_0^2|S^{n-1}| \int_{\mathbb{R}^n} |\omega|^{4\gamma} |\mathcal{F}(\tilde{\eta}_z^h)(\omega)|^2 d\omega + \mathcal{O}(h).$$

*Proof.* Recalling the numerator of our proposed index function in (2.16), we can rewrite it as

$$\langle u_s, \eta_z^h \rangle_\gamma = \int_{\mathbb{R}^n} (-\Delta)^\gamma u_s \tilde{\eta}_z^h dx + \int_{\mathbb{R}^n} (-\Delta)^\gamma u_s [\eta_z^h - \tilde{\eta}_z^h] dx.$$

Since  $Rf \in L^\infty(S^{n-1} \times \mathbb{R})$ , the expectation of the product of measurements is given by

$$(3.27) \quad \begin{aligned} \mathbb{E}[u_s(x)u_s(y)] &= \int_{S^{n-1} \times S^{n-1}} \left[ Rf_e(\alpha, \alpha \cdot x) Rf_e(\beta, \beta \cdot y) + \sigma_0^2 \delta(\alpha - \beta) \delta(\alpha \cdot x - \beta \cdot y) \right] d\alpha d\beta \\ &= u_e(x)u_e(y) + |S^{n-1}|^2 \sigma_0^2 \delta(x - y), \end{aligned}$$

where  $u_e$  represents the exact value, and  $u_s$  is the measurement data with noise. From the above, we see the expectation for  $z \in \Omega$  is

$$(3.28) \quad \mathbb{E}[I_\gamma^h(z)] = \frac{\int_{\mathbb{R}^n} u_s (-\Delta)^\gamma \tilde{\eta}_z^h dx + \phi_1(z)}{n(z)},$$

where  $\phi_1(z)$  is defined in (3.15). By Lemma 2.1(c),  $(-\Delta)^\gamma \tilde{\eta}_z^h$  belongs to  $L^2(\mathbb{R}^n)$ . Then one can finally derive the relationship between the variance of the index function and the Sobolev scale  $\gamma$ :

$$(3.29) \quad \begin{aligned} & [n(z)\sigma_\gamma(z)]^2 + \phi_1(z) \\ &= \int_{\mathbb{R}^n \times \mathbb{R}^n} \left[ \mathbb{E}[u_s(x)u_s(y)] (-\Delta)^\gamma \tilde{\eta}_z^h(x) (-\Delta)^\gamma \tilde{\eta}_z^h(y) \right] dx dy - \left[ \int_{\mathbb{R}^n} \mathbb{E}[u_s] (-\Delta)^\gamma \tilde{\eta}_z^h dx \right]^2 \\ &= \sigma_0^2 |S^{n-1}| \int_{\mathbb{R}^n} |(-\Delta)^\gamma \tilde{\eta}_z^h|^2 dx = \sigma_0^2 |S^{n-1}| \int_{\mathbb{R}^n} |\omega|^{4\gamma} |\mathcal{F}(\tilde{\eta}_z^h)(\omega)|^2 d\omega. \end{aligned}$$

By the estimate in (3.16), we know  $\phi_1(z) \leq \|(-\Delta)^{\gamma-\frac{1}{2}} f\|_{L^\infty(\mathbb{R}^n)} h$ , hence the magnitude of  $\phi_1(z)$  is of the order  $\mathcal{O}(h)$ . Now, we have the desired conclusion of the lemma.  $\blacksquare$

We now substitute the representation of the normalization term  $n(z)$  defined in (2.16) into (3.29). In Figure 2, assuming  $\Omega = [-0.5, 0.5]^n$  for  $n = 2$  (left) and  $n = 3$  (right) with  $h = 0.025$ , we plot the natural logarithm of the variance of the index function at the origin, i.e.,  $\ln(\sigma_\gamma^2(0))$ , with respect to  $\gamma \in [0.2, 0.975]$  where the step size of  $\gamma$  equals to 0.025. The constant  $\sigma_0$  in

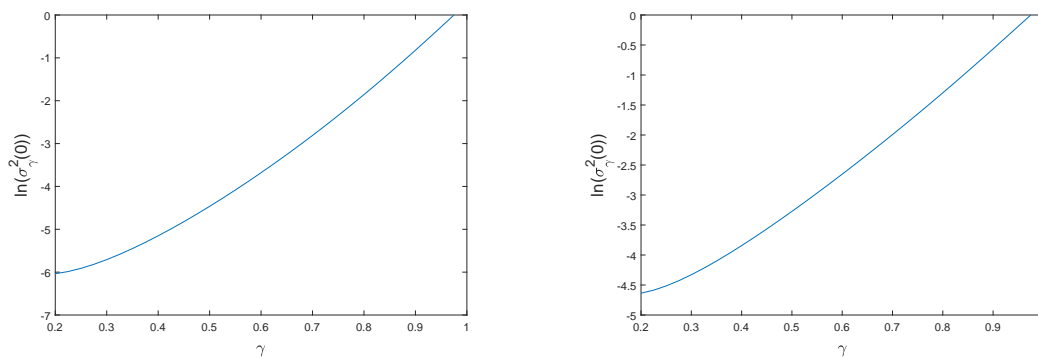


**Figure 2.**  $\ln(\sigma_\gamma^2(0))$  (cf. (3.28)) with respect to  $\gamma \in [0.2, 0.975]$  in  $\mathbb{R}^2$  (left) and in  $\mathbb{R}^3$  (right).

(3.29) is chosen such that  $\max_{\gamma \in [0.2, 0.975]} \sigma_\gamma^2(0) = 1$  for all  $\gamma$ . Our computation only considers  $\gamma \geq 0.2$  is due to (3.21), which implies the accuracy of the reconstruction is not satisfactory for relatively small  $\gamma$ . From Figure 2, for both reconstructions in  $\mathbb{R}^2$  and  $\mathbb{R}^3$ , the variance of the index function increases exponentially with respect to  $\gamma$ . Hence, we shall not consider the possibility of very large  $\gamma$ , i.e.,  $\gamma \geq n/2$ , in real applications. This conclusion is also consistent with the motivation of DSM in section 2 that we expect a smaller choice of the Sobolev scale  $\gamma$  will improve the robustness of the reconstruction under high level of random noise.

We end this section with a summary of our theoretical predictions on the appropriate choice of the Sobolev scale  $\gamma$  for applications, based on the discussions in sections 3.3 and 3.4. For the reconstruction from noisy and inadequate measurement data that we are particularly interested in, we shall choose  $\gamma$  that is relatively small considering the relationship revealed in Figure 2. Moreover, for  $\gamma > 0$  but much smaller than  $(n-1)/2$ , from (3.21) in section 3.3, the reconstruction results may not be accurate enough. Hence, we may prefer to choose  $\gamma$  that is close to  $(n-1)/2$  for our DSM, for instance,  $\gamma = 0.4$  in  $\mathbb{R}^2$  and  $\gamma = 0.9$  in  $\mathbb{R}^3$ . This theoretical prediction will be verified in Example 1 of section 6.

**4. DSMs for some other tomography problems.** As we pointed out in section 3, the new DSM is expected to be robust against noise, due to the property of the probing function as a low pass filter and the choice of the duality product which avoids applying any pseudo-differential operator on the noisy measurement data. Therefore, we are interested in whether the DSM also performs reasonably in the limited angle tomography, which is another closely related and highly ill-posed inverse problem associated with the Radon transform.

We will focus on the two-dimensional case when detectors are distributed in the parallel geometry. Recall the Radon transform for a smooth target function  $f$ :

$$Rf(\theta, t) = \int_{x \cdot \theta = t} f(x) dx_L, \quad \theta \in S^1, \quad t \in \mathbb{R},$$

where we assume  $\theta \in [-\Phi, \Phi]$  for  $\Phi < \pi/2$ , and  $s \in I_\theta$ , with  $I_\theta$  being the same as in (2.2). In this case, the dual of the Radon transform with limited angle measurement is given by

$$(4.1) \quad R_\Phi^* g(x) := \int_{S^1} g(\theta, x \cdot \theta) \mathcal{X}_{V_\Phi}(\theta) d\theta, \quad V_\Phi = [-\Phi, \Phi] \cup [\pi - \Phi, \pi + \Phi],$$

where  $\mathcal{X}_V(\theta) = 1$  if  $\theta \in V$  and  $\mathcal{X}_V(\theta) = 0$  otherwise.

The limited angle tomography will be very different from the case where we have measurements from all directions as in section 2. In particular, the extra discontinuity of the characteristic function in (4.1) will create undesirable artifacts when we apply a pseudodifferential operator on the measurement data, including the proposed fractional Laplacian. A classification of artifacts was deduced in the work [14] with an argument using microlocal analysis and the wavefront set.

If we employ the same index function as in (2.16), with  $u_s$  replaced by  $u_s^\Phi = 1/2R_\Phi^*Rf$ , the numerator of the index function becomes

$$(4.2) \quad \langle u_s^\Phi, \eta_z^h \rangle_\gamma = \int_{\mathbb{R}^2} u_s^\Phi (-\Delta)^\gamma \eta_z^h(x) dx.$$

We now consider the above duality product in the frequency domain. Recalling the Fourier slice theorem, i.e.,  $\mathcal{F}_t(Rf)(\theta, t) = \mathcal{F}(f)(t\theta)$ , where  $\mathcal{F}_t$  is the one-dimensional Fourier transform with respect to  $t$ , we can rewrite  $u_s^\Phi$  as

$$(4.3) \quad \begin{aligned} u_s^\Phi(x) &= \int_{\mathbb{S}^1} \mathcal{F}_t^{-1}\{\mathcal{F}_t Rf\}(\theta, x \cdot \theta) \mathcal{X}_{V_\Phi}(\theta) d\theta = \int_{\mathbb{S}^1} \int_{\mathbb{R}} \mathcal{F}(f)(\theta\tau) e^{2\pi i\tau(x \cdot \theta)} d\tau \mathcal{X}_{V_\Phi}(\theta) d\theta \\ &= \int_{\mathbb{R}^2} \mathcal{F}(f)(\omega) \frac{\mathcal{X}_{V_\Phi}(\omega/|\omega|)}{|\omega|} e^{2\pi i\omega \cdot x} d\omega = \left( f * \mathcal{F}^{-1} \left( \frac{\mathcal{X}_{V_\Phi}(\omega/|\omega|)}{|\omega|} \right) \right)(x). \end{aligned}$$

Hence, the duality product between the measurement data and the probing function with a small choice of the Sobolev scale  $\gamma < 1/2$  becomes

$$(4.4) \quad \langle u_s^\Phi, \eta_z^h \rangle_\gamma = \mathcal{F}^{-1} \left( \mathcal{X}_{V_\Phi}(\omega/|\omega|) |\omega|^{2\gamma-1} \mathcal{F}(\tilde{\eta}_0^h) \mathcal{F}(f) \right)(z) + \int_{\mathbb{R}^2} (-\Delta)^\gamma u_s^\Phi (\tilde{\eta}_z^h - \eta_z^h) dx,$$

where the order of the second integration in the right-hand side is  $\mathcal{O}(h)$  with an estimate similar to (3.4). In this case, the duality product with a relatively small Sobolev scale combining with the probing function will serve as a low pass filter in the frequency domain to improve the numerical stability of the reconstruction.

Similarly to [14], we can further employ the modified back projection operator to improve the accuracy of the reconstruction:

$$(4.5) \quad \tilde{R}_\Phi^* g(x) := \int_{\mathbb{S}^1} g(\theta, x \cdot \theta) \Psi_{V_\Phi}(\theta) d\theta,$$

where  $\Psi_{V_\Phi}$  is defined as (with  $\lambda$  being a fixed value representing the range of data that is smoothed)

$$\Psi_{V_\Phi}(\theta) = \begin{cases} 1, & \theta \in [-\Phi, \Phi] \cup [\pi - \Phi, \pi] \cup [-\pi, -\pi + \Phi]; \\ 1 - \frac{|\theta - \Phi|}{\lambda}, & \theta \in [-\Phi - \lambda, -\Phi) \cup (\Phi, \Phi + \lambda]; \\ 1 - \frac{(\pi - \Phi) - |\theta|}{\lambda}, & \theta \in [\pi - \Phi - \lambda, \pi - \Phi) \cup (-\pi + \Phi, -\pi + \Phi + \lambda]; \\ 0 & \text{otherwise.} \end{cases}$$

This modified back projection operator smooths the original characteristic function  $\mathcal{X}_{V_\Phi}$  that appears in (4.1) to a piecewise linear function. We plot the values of  $\Psi_{V_\Phi}(\theta)$  in Figure 3 for

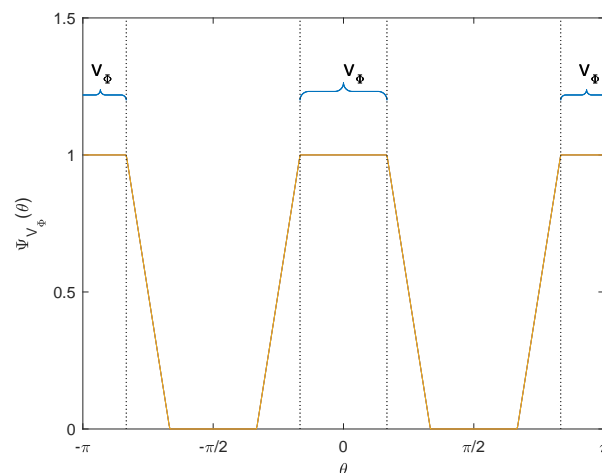


**Figure 3.** Values of  $\Psi_{V_\Phi}(\theta)$  (cf. (4.5)) with  $V_\Phi = [-\pi/6, \pi/6]$  and  $\lambda = \pi/6$ , where  $V_\Phi$  is the range of angles for that the projection data is available.

$V_\Phi = [-\pi/6, \pi/6]$  and  $\lambda = \pi/6$ . The realization of  $\Psi_{V_\Phi}$  is achieved by a direct extension of the measurement data.

To conclude, the index function for reconstructing  $f$  at the sampling point  $z$  reads now as

$$(4.6) \quad I_h^\gamma(z) = \frac{\langle u_s^\Phi, \eta_z^h \rangle_\gamma}{n(z)} \quad \text{with} \quad u_s^\Phi = \frac{1}{2} \tilde{R}_\Phi^* R f \quad \text{and} \quad n(z) = \left\langle \frac{1}{2} R^* R(\mathbb{1}_\Omega), \eta_z^h \right\rangle_\gamma.$$

We shall demonstrate the robustness of the DSM in this limited angle tomography numerically in Example 5 of section 6.

Furthermore, our above discussion applies to the case that the measurement is in the fan beam geometry when the range of measurement angles is limited. The proposed index function can be employed after replacing  $u_s^\Phi$  in (4.6) by the back-projected data obtained from the fan beam measurement.

We end this section with a discussion of the application of the DSM to a special inverse problem of the exponential Radon transform. The exponential Radon transform appears in the radionuclide imaging and can be regarded as a generalization of the Radon transform [37].

First, assuming  $f$  is smooth and compactly supported in  $\Omega$ , we denote  $T_\mu f(\theta, t)$  and  $T_\nu^* g(x)$  as

$$(4.7) \quad T_\mu f(\theta, t) := \int_{\mathbb{R}^n} f(x) e^{\mu x \cdot \theta^\perp} \delta(t - x \cdot \theta) dx, \quad T_\nu^* g(x) := \int_{S^{n-1}} g(\theta, \theta \cdot x) e^{\nu x \cdot \theta^\perp} d\theta$$

for  $x \in \mathbb{R}^n$ ,  $\theta \in S^{n-1}$ , and  $t \in \mathbb{R}$ . We note that  $\theta^\perp$  can be defined through a fixed rotation rule, for instance, rotating  $\theta$  clockwise for  $\pi/2$  in  $\mathbb{R}^2$ . The Radon transform is a special case of (4.7) with  $\mu = 0$ . With a change of variable, the measurement data after back projection becomes

$$(4.8) \quad u^\mu(x) := T_\mu^* T_{-\mu} f(x) = \int_{\mathbb{R}^n} \int_{S^{n-1}} f(y) e^{\mu(y-x) \cdot \theta^\perp} \delta(y \cdot \theta - x \cdot \theta) d\theta dy = \int_{\mathbb{R}^n} f(y) \frac{e^{\mu|x-y|}}{|x-y|} dy.$$

Considering a special case of the exponential Radon transform, that is,  $n = 3$  and  $\mu = ik$  with  $k > 0$ ,

$$(4.9) \quad u^{ik}(x) = T_{ik}^* T_{-ik} f(x) = \int_{\Omega} f(y) \frac{e^{ik|x-y|}}{|x-y|} dy = (f * \tilde{G}_0)(x),$$

where  $\tilde{G}_x$  satisfies  $(\Delta + k^2)\tilde{G}_x = 4\pi\delta_x$ . Hence, an inversion formula for the measurement is

$$(4.10) \quad f(x) = (4\pi)^{-1}(\Delta + k^2)u^{ik}(x).$$

We observe that, with the index function defined in (2.16),  $f(x)$  can be reconstructed by employing  $\tilde{I}(x) = I_{\gamma}^h(x) + k^2 u^{ik}(x)$  and all our early discussions could be extended to this scenario.

**5. Numerical implementations.** In this section, we introduce some numerical implementations of the proposed DSM, especially the evaluation of the duality product (2.5) between the measurement data and the probing function. With several strategies that are employed to reduce the computational time of our method, we will compare the computational complexity of DSM with the popular FBP method.

We first recall the definition of the index function in (2.16); since both  $(-\Delta)^{\gamma}\eta_z^h$  and  $f$  are contained in  $L^2(\mathbb{R}^n)$ , the numerator of  $I_{\gamma}^h(z)$  can be written as

$$(5.1) \quad \begin{aligned} \langle u_s, \eta_z^h \rangle_{\gamma} &= d_n \int_{\mathbb{R}^n} R^* R f(x) (-\Delta)^{\gamma} \eta_z^h dx = d_n \int_{\mathbb{R}^n} \left[ \int_{\mathbb{S}^{n-1}} R f(\theta, x \cdot \theta) d\theta \right] (-\Delta)^{\gamma} \eta_z^h(x) dx \\ &= d_n \int_{\mathbb{S}^{n-1}} \left[ \int_{\mathbb{R}^n} R f(\theta, x \cdot \theta) (-\Delta)^{\gamma} \eta_z^h(x) dx \right] d\theta. \end{aligned}$$

Now we investigate more carefully the integration of the product between the Radon transform of the target function  $f$  and the fractional Laplacian of the probing function in  $\mathbb{R}^n$ . We first notice that if  $\text{supp}\{f\} \subseteq \Omega \subseteq B(0, r_2)$ , then  $Rf(\theta, t) = 0$  for  $|t| > r_2$ . With this observation, we know the integral part with respect to  $\theta$  in (5.1) equals to

$$(5.2) \quad \begin{aligned} \int_{\mathbb{R}^n} R f(\theta, x \cdot \theta) (-\Delta)^{\gamma} \eta_z^h(x) dx &= \int_{\mathbb{R}} \int_{x \cdot \theta = t} (-\Delta)^{\gamma} \eta_z^h(x) R f(\theta, t) dx dt \\ &= \int_{|t| < r_2} R((-\Delta)^{\gamma} \eta_0^h)(\theta_0, t - z \cdot \theta) R f(\theta, t) dt \\ &= \int_{|t| < r_2} (-\Delta_{t-\tau})^{\gamma} R(\eta_0^h)(\theta_0, t - \tau) R f(\theta, t) dt \end{aligned}$$

for a fixed angle  $\theta_0$ , where we have employed in the second equality of (5.2) the following property regarding the Radon transform for an arbitrary radial function  $g_0 \in L^2(\mathbb{R}^n)$  that satisfies  $g_0(x) = g_0(|x|)$  and  $g_z(x) = g(x - z)$ :

$$R(g_z)(\theta, t) = R(g_0)(\theta_0, t - z \cdot \theta)$$

for a fixed angle  $\theta_0$  and arbitrary angles  $\theta$ . The last equality in (5.2) holds due to the intertwining property between the fractional Laplacian and the Radon transform, which can be derived through the Fourier slice theorem, i.e.,  $\mathcal{F}_t(Rf)(\theta, t) = \mathcal{F}(f)(t\theta)$ , and the representation of the fractional Laplacian through a Fourier multiplier.

For notational reasons, we define  $H(\theta, \tau) := \int_{|t| < r_2} (-\Delta_{t-\tau})^\gamma R(\eta_0^h)(\theta_0, t - \tau) Rf(\theta, t) dt$ . Then (5.1) can be computed by

$$\langle u_s, \eta_z^h \rangle_\gamma = d_n R^*(H(\theta, \tau))(z).$$

To summarize, the implementation of the DSM for reconstructing the target function  $f$  consists of the following steps:

- In the off-line computation, for a set of discrete sampling point  $z_j \in \Gamma_z \subset \Omega \subseteq B(0, r_2)$ , we take  $h = \min_{z_i, z_j \in \Gamma_z} |z_i - z_j|$ . Then we choose a set of uniformly distributed points

$$\Gamma_\tau = \{\tau_k = -r_2 + hk; hk < 2r_2 + h, k \in \mathbb{N}\} \subset \mathbb{R}$$

and compute  $(-\Delta_\tau)^\gamma R(\eta_0^h)(\theta_0, \tau_k)$  with  $\theta_0 = 0$  and  $\tau_k \in \Gamma_\tau \cup r_2 + \Gamma_\tau \cup -r_2 + \Gamma_\tau$ . Finally, for each sampling point  $z_j$ , we compute  $n(z_j)$  defined in (2.16).

- Given the measurement data  $Rf(\theta_i, t_j)$  with measurement angles  $\theta_i \in \Gamma_\theta \subset \mathbb{S}^{n-1}$  and discrete measurement points  $t_j \in \Gamma_t(\theta) \subset I_\theta \subset \mathbb{R}$  defined by (2.2),
  1. for each  $\theta_i \in \Gamma_\theta, \tau_k \in \Gamma_\tau$ , we compute

$$(5.3) \quad H(\theta_i, \tau_k) = h \sum_j (-\Delta_{t-\tau})^\gamma R(\eta_0^h)(\theta_0, t_j - \tau_k) Rf(\theta_i, t_j);$$

2. for each sampling point  $z_j$ , we apply the back projection operator  $R^*$  on  $H(\theta_i, \tau_k)$  to obtain  $\langle u_s, \eta_{z_j}^h \rangle_\gamma$ . Then we divide it by  $n(z_j)$  to obtain the index function  $I_\gamma^h(z_j)$  which recovers the target function  $f(z_j)$ .

**Comparison between computational complexities of DSM and FBP.** We now recall the implementation of the FBP method, which applies the ramp filter composed with a proper low pass filter on the  $t$  variable of  $Rf(\theta, t)$ , and then back-projecting it to recover  $f$ . In general, for the standard case that measurement points  $t_j$  are uniformly distributed, the step of filtering in an FBP reconstruction requires  $\mathcal{O}(N \log N)$  flops for  $N$  discretization points. Considering the computational complexity of our DSM, except for the step of back projection that we share with the FBP method, the method requires only two extra steps. The first is to compute  $H(\theta, \tau)$  with (5.3). In this step, we can observe that the matrix representation of  $(-\Delta_{t-\tau})^\gamma R(\eta_0^h)(\theta_0, t_j - \tau_k)$  is a Toeplitz matrix since the value of entries only depends on  $t_j - \tau_k$ . Hence, with the fast Fourier transform, the computation of (5.3) costs  $\mathcal{O}(N \log N)$  flops. The second extra step required by DSM is to divide the duality product by the normalization term  $n(z_j)$  which only costs  $\mathcal{O}(N)$  flops. To conclude, the overall computational complexity of the DSM is of the same order as the traditional FBP method. However, as we shall observe from a series of numerical experiments in section 6, DSM provides more robust and accurate reconstructions. We mention that the traditional methods which yield reasonable reconstructions in those challenging situations have much higher computational complexities; for instance, they often involve minimizing a functional with certain regularization [16].

**Comparison between DSM and methods with total variation regularization.** Another popular approach in solving Radon inverse problems is least-square minimization with TV regularization. In particular, we think the proposed DSM and the minimization

approach with TV penalty may be better considered as two numerical methods that are suitable for different purposes. First, the reconstruction with TV penalization should be much more computationally intensive compared with the DSM, as one needs to minimize a nonlinear and nonsmooth functional formed by a data-fitting term and a TV regularization. This is often solved by an appropriate iterative method. This solution process is a global minimization and appears hard to do in parallel.

In contrast, DSMs do not require any iterative procedure and can be implemented in a highly parallel manner to further improve its efficiency as introduced earlier. Furthermore, DSMs do not require any prior information that is usually key to the success of regularization type methods.

Nevertheless, it would be interesting to combine the regularization type methods with DSMs to further improve the reconstructions of DSMs. As we will see from numerical experiments in section 6, even for the cases with very noisy or inadequate measurement data, the reconstructions from DSM provide very good geometrical and physical approximations of the unknown targets. Therefore, we may use the fast and robust reconstructions from DSM as a reasonable initial guess for the regularization type methods; see the numerical Example 5 in section 6.

**6. Numerical experiments.** A series of numerical experiments are carried out in this section to illustrate the robustness and accuracy of the novel DSM for a number of representative applications in two and three dimensions. For two-dimensional experiments, we take the sampling domain  $\Omega = [-0.5, 0.5] \times [-0.5, 0.5]$ , with the mesh size  $h = 5 \times 10^{-3}$ . Detectors are placed in parallel arrays and the angular increment is 0.25 degree except for Examples 3 and 5.

In the first five examples, the Radon transform of the target function  $f$  supported in  $\Omega$  is available at a set of discrete angles  $\Gamma_\theta$ , which are uniformly distributed in  $[-\pi/2, \pi/2)$  (except for Examples 4 and 5) and at discrete points  $\Gamma_t(\theta) \subset I_\theta$  defined by (2.2). For each example, the number of projection data collected equals to  $284 \times N_\theta$ , where  $284 \approx 200\sqrt{2}$  is the number of data collected in each angle that is chosen to cover the convex hull of  $\Omega$  and  $N_\theta$  represents the number of projection angles. For a summary of discretization parameters, we refer to Table 1. Two original images are examined, with the first one being an image containing four objects with different shapes, and the second one being the classical head phantom image.

Additive Gaussian random noises are added to the Radon transform of  $f$  in all experiments:

$$(6.1) \quad Rf_s(\theta, t) := Rf_e(\theta, t) + \epsilon\delta, \quad \theta \in \Gamma_\theta, \quad t \in \Gamma_t(\theta),$$

where  $\epsilon$  is the standard normal distribution,  $Rf_e$  is the exact data, and  $\delta = \text{mean}(Rf_e) \times$  (noise level).

**Table 1**

*Summary of discretization parameters in  $\mathbb{R}^2$  for Examples 1 to 5.*

Domain of reconstruction ( $\Omega$ )	$[-0.5, 0.5] \times [-0.5, 0.5]$
Mesh size of discretization ( $h$ )	0.005
Number of discretization points ( $N$ )	$40101 = (201)^2$
Number of projection angles ( $N_\theta$ )	$10 \leq N_\theta \leq 720$
Number of projection data collected	$284 \times N_\theta$

In each of the following examples, we first generate the exact measurement data  $Rf_e(\theta, t)$  and then impose the noise on the exact data as in (6.1) to obtain  $Rf_s(\theta, t)$ . Then the index function (2.16) is evaluated with the basic computational strategies introduced in section 5. To compare DSM with existing methods, we choose the FBP method with the Hamming filter for reconstructing the images. This corresponds to adding the Hamming window on the classical ramp filter.

To compare the numerical reconstruction qualities, we compute the mean square error (MSE),  $L^\infty$ -norm error ( $\text{Err}^\infty$ ), peak signal to noise ratio (PSNR), and structural similarity index (SSIM) of the reconstruction by different methods, respectively. We denote by  $I_r$  the image reconstructed by the new DSM or the FBP method or the regularization type method, and by  $I_O$  the original image. We denote  $\mu_r, \sigma_r$  as the mean and the standard deviation of  $I_r$ , and  $\sigma_{r,O}$  as the covariance of  $I_r$  and  $I_O$ . With the set of sampling points  $\{z_j\}_{1 \leq j \leq N} = \Omega^N \subset \Omega$ , we then define

$$(6.2) \quad \begin{aligned} \text{MSE} &:= \frac{1}{N^2} \sum_{z_j \in \Omega^N} |I_r(z_j) - I_O(z_j)|^2, & \text{Err}^\infty &:= \frac{\max_{z_j \in \Omega^N} \{|I_r(z_j) - I_O(z_j)|\}}{\max_{z_j \in \Omega^N} \{|I_O(z_j)|\}}, \\ \text{PSNR} &:= 10 \log_{10} \left( \frac{1}{\text{MSE}} \right), & \text{SSIM} &:= \frac{(2\mu_r \mu_O + c_1)(2\sigma_{r,O} + c_2)}{(\mu_r^2 + \mu_O^2 + c_1)(\sigma_r^2 + \sigma_O^2 + c_2)}, \end{aligned}$$

where  $c_1 = 0.01^2$  and  $c_2 = 0.03^2$  are constants to avoid instability in computations. We remark that a better reconstruction is expected to have smaller MSE,  $\text{Err}^\infty$  and larger PSNR, SSIM. Moreover, we also report the CPU times in seconds for executing numerical algorithms on an AMD Ryzen 7 4800HS CPU in MATLAB R2020B to compare the efficiency of different reconstruction methods.

To fairly compare the reconstruction quality of DSM, FBP, and the regularization type method, we plot the normalized index function  $\tilde{I}_r(z)$  for each reconstruction that is defined to be  $\tilde{I}_r(z) = I_r(z) / \max_{y \in \Omega^N} |I_r(y)|$ . In all figures, images in the same row are generated with the same measurement data to demonstrate certain numerical phenomena; plots with subtitles DSM, FBP, TV, and  $f(x)$  are the reconstructions by DSM, FBP, the least-square method with TV, and the original image being recovered.

*Example 1.* We examine in this example the influence of the Sobolev scale  $\gamma$  (cf. (2.5)) and parameter  $\alpha$  (cf. (2.8)) on the reconstruction to validate our previous theoretical predictions and also to provide some important practical guidance on their choice for the subsequent examples. Reconstructions by DSM (with  $\gamma = 0.3, 0.4, 0.5, 0.6$ ) and reconstructions by DSM (with  $\alpha = 3, 4, 5$ ) are shown in Figure 4.

We compute the four images in the first row of Figure 4 with the same measurement data under different choices of  $\gamma = 0.3, 0.4, 0.5$ , and  $0.6$  with  $\alpha = 3$  and 20% additive Gaussian noise. We may observe that the reconstruction is sharper but less stable as  $\gamma$  increases. Denoting  $\text{MSE}_{\gamma=\lambda}$  as the MSE of the reconstruction by DSM with  $\gamma = \lambda$  as in (6.2), then the corresponding reconstruction errors are given by

$$\text{MSE}_{\gamma=0.3} = 0.171, \quad \text{MSE}_{\gamma=0.4} = 0.135, \quad \text{MSE}_{\gamma=0.5} = 0.153, \quad \text{MSE}_{\gamma=0.6} = 0.342.$$

The above numerical results follow from our previous theoretical conclusions at the end of section 3.4 that we expect a smaller  $\gamma$  will provide more stable reconstruction results with

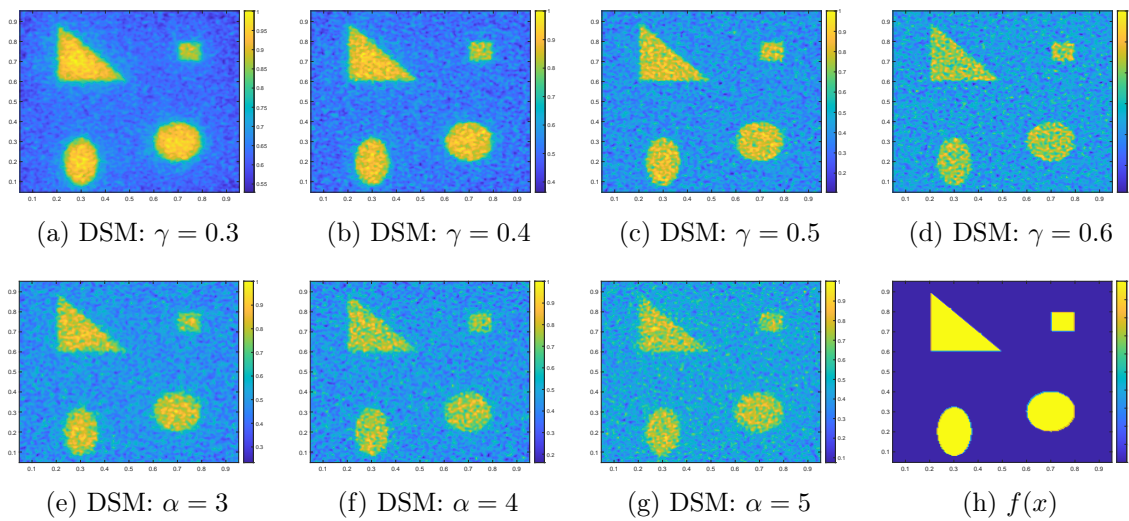


**Figure 4.** Example 1. Influence of choices of  $\gamma$  and  $\alpha$ : reconstruction by DSM under 20% additive Gaussian noise and  $\alpha = 3$  with  $\gamma = 0.3, 0.4, 0.5,$  and  $0.6$  (first row); reconstruction by DSM under 30% additive Gaussian noise and  $\gamma = 0.4$  with  $\alpha = 3, 4, 5$  and the original image (second row).

noisy measurement data, i.e., comparing  $\gamma = 0.4, 0.5,$  and  $0.6,$  but at the same time, the reconstruction is not accurate enough for  $\gamma$  that is too small, i.e., comparing  $\gamma = 0.3$  and  $0.4.$  Hence, for the following examples, we will mainly employ  $\gamma = 0.4$  to enhance both the numerical stability and the accuracy of the reconstruction. Moreover, to illustrate the feasibility of the proposed DSM with other choices of  $\gamma,$  we also employ  $\gamma = 0.55$  in the second case of Example 2 to demonstrate that our method performs stably for a wide range of  $\gamma$  due to the choice of the probing function which serves as a low pass filter as we discussed in section 3.3.

Next, we would like to justify our preference of choosing  $\alpha = n + 1$  ( $\alpha = 3$  in  $\mathbb{R}^2$ ) for reconstruction. We compute the first three images in the second row with the same measurement data under different choices of  $\alpha = 3, 4,$  and  $5$  with  $\gamma = 0.4$  and 30% additive Gaussian noise. Denoting  $\text{MSE}_{\alpha=\lambda}$  as the MSE of the reconstruction with  $\alpha = \lambda,$  then the corresponding reconstruction errors are given by

$$\text{MSE}_{\alpha=3} = 0.151, \quad \text{MSE}_{\alpha=4} = 0.173, \quad \text{MSE}_{\alpha=5} = 0.189.$$

We observe that the reconstruction becomes less accurate as  $\alpha$  becomes larger under high level Gaussian noise. The above observation echoes with the analysis in section 3.2. This suggests the choice of  $\alpha = 3$  in most real applications, namely,  $\alpha = n + 1$  in  $\mathbb{R}^n$  as justified in section 3.2.

*Example 2.* This example involves additive Gaussian noise in the data. The reconstructions by DSM (with  $\gamma = 0.4$  in the first row and with  $\gamma = 0.55$  in the second row) and FBP are shown in Figure 5. The corresponding indicators measuring reconstruction qualities are listed in the tables

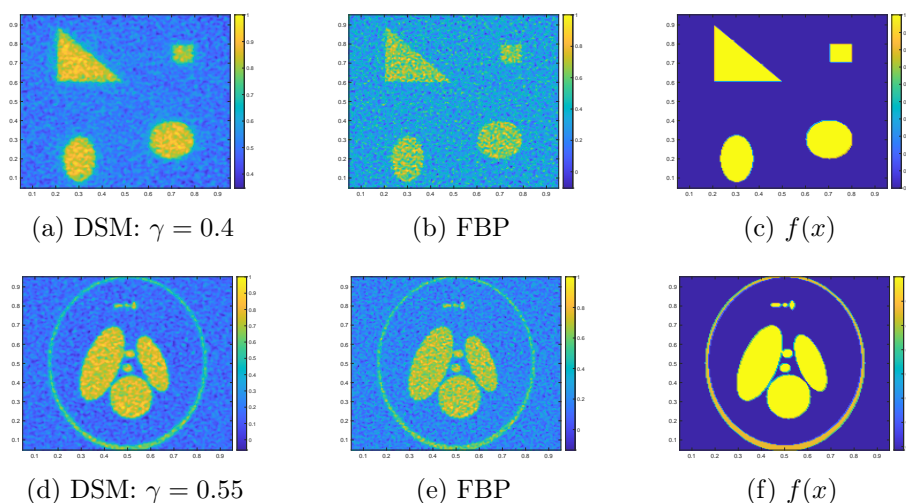


Figure 5. Example 2. Under additive Gaussian noise: 20%.

Method	MSE	$\text{Err}^\infty$	PSNR	SSIM	CPU time (s)
DSM	0.234	0.188	18.774	0.293	0.075
FBP	0.274	0.210	17.4111	0.223	0.103

for the reconstructions with the noise level being 20% (the first row of Figure 5) and

Method	MSE	$\text{Err}^\infty$	PSNR	SSIM	CPU time (s)
DSM	0.135	0.139	21.948	0.486	0.136
FBP	0.293	0.248	15.237	0.086	0.366

for the reconstructions with the noise level being 20% (the second row of Figure 5).

From the numerical reconstructions, we can observe that the DSM is very robust against strong Gaussian noise in the measurement data. And based on the  $L^2$ -norm error and the  $L^\infty$ -norm error of the reconstruction, we can see that the DSM performs obviously better than FBP.

*Example 3.* This example studies a relatively challenging case with a limited number of projection angles in  $\Gamma_\theta$ , sparsely distributed over  $[-\pi/2, \pi/2)$ . The reconstructions by DSM (with  $\gamma = 0.4$ ) and FBP are shown in Figure 6. The corresponding indicators measuring reconstruction qualities are listed in the tables

Method	MSE	$\text{Err}^\infty$	PSNR	SSIM	CPU time (s)
DSM	0.166	0.219	20.169	0.298	0.008
FBP	0.473	0.701	11.076	0.048	0.008

for the reconstruction with projections from 18 angles (the first row of Figure 6) and

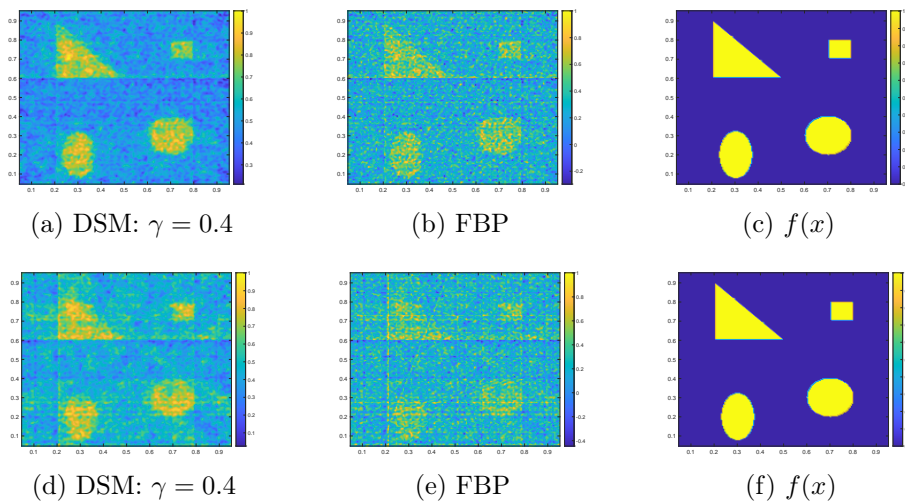


**Figure 6.** Example 3. Sparse measurements with 5% additive Gaussian noise.

Method	MSE	Err <sup>∞</sup>	PSNR	SSIM	CPU time (s)
DSM	0.213	0.235	17.987	0.199	0.008
FBP	0.663	0.857	8.136	0.029	0.005

for the reconstruction with projections from 10 angles (the second row of Figure 6).

As we may see from the reconstructions, the DSM demonstrates its strong robustness in this highly ill-posed scenario especially with respect to the  $L^\infty$ -norm error of the reconstruction. Moreover, for reconstructions in the second row with projections only from 10 directions, DSM still allows us to identify the shape and the location of objects in a reasonable manner, while it is difficult to obtain useful information from the reconstruction by the FBP method. This shows the great potential of the DSM in real applications when projection angles are very sparsely distributed.

*Example 4.* In this example, we consider the projection angles limited to a specific range as in section 4. The back projection operator needed in both the DSM and FBP reconstructions takes the form (4.5) with  $\lambda = \pi/18$ . The reconstructions by DSM (with  $\gamma = 0.4$ ) and FBP are shown in Figure 7. The corresponding indicators measuring reconstruction qualities are listed in the tables

Method	MSE	Err <sup>∞</sup>	PSNR	SSIM	CPU time (s)
DSM	0.179	0.174	19.525	0.643	0.063
FBP	0.270	0.232	15.939	0.142	0.065

for the reconstruction with  $\Phi = \pi/3$  (the first row of Figure 7) and

Method	MSE	Err <sup>∞</sup>	PSNR	SSIM	CPU time (s)
DSM	0.217	0.213	17.836	0.552	0.043
FBP	0.350	0.328	13.699	0.100	0.061

for the reconstruction with  $\Phi = 2\pi/9$  (the second row of Figure 7).

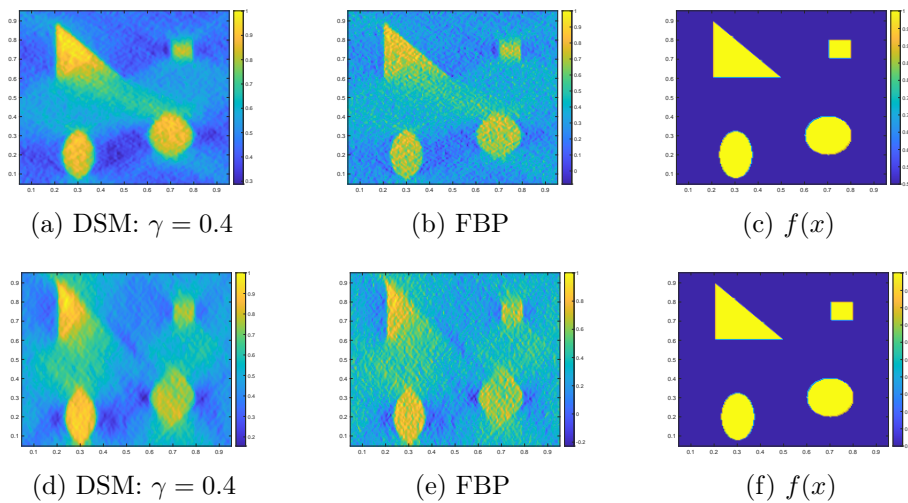


**Figure 7.** *Example 4. Limited angle tomography, with 10% additive Gaussian noise: reconstructions with  $\Phi = \pi/3$  (first row) and  $\Phi = 2\pi/9$  (second row).*

As we may see from the numerical reconstructions, especially from the second case where the projections are restricted only on a very narrow range with  $\Phi = 2\pi/9$ , the DSM performs obviously better than FBP, based on the MSE and the  $L^\infty$ -norm error of the reconstruction. As we can see from Figure 7(a), the shape of objects is recovered more accurately compared with FBP.

*Example 5.* In this example, we consider the comparison and the combination of the novel DSM with least-square methods with TV regularization for the sparse tomography and limited angle tomography with 5% additive Gaussian noise. In particular, we are interested in the speed-up of the convergence of the minimization of the target functional if we use the reconstruction by DSM as an initial guess for the minimization process. The functional to be minimized is of the form  $\|RI_{TV} - Rf\|_2^2/2 + \alpha \int_{\Omega} |\nabla I_{TV}| dx$ , where  $Rf$  is the noisy measurement data,  $I_{TV}$  is the reconstruction, and  $\alpha$  is the TV regularization parameter. To minimize the target functional, we follow the practical implementation of the Nesterov's optimal first order method in [20] and choose  $\alpha = 50$  to reconstruct the piecewise constant original image more efficiently. The iteration terminates when the norm of an approximate gradient map is smaller than  $10^{-2}$ ; we refer to [20] for more details and report the number of iterations required in the following table when the TV approach is employed.

From left to right, the reconstructions by DSM (with  $\gamma = 0.4$ ), FBP, least-square method with TV regularization (but with the reconstruction by DSM as the initial guess), and  $R^*Rf$  (unfiltered backprojection) that is a common choice in practice as the initial guess are shown in Figure 8, respectively. The corresponding indicators measuring reconstruction qualities of different methods and the number of iterations required for the minimization are listed in the tables

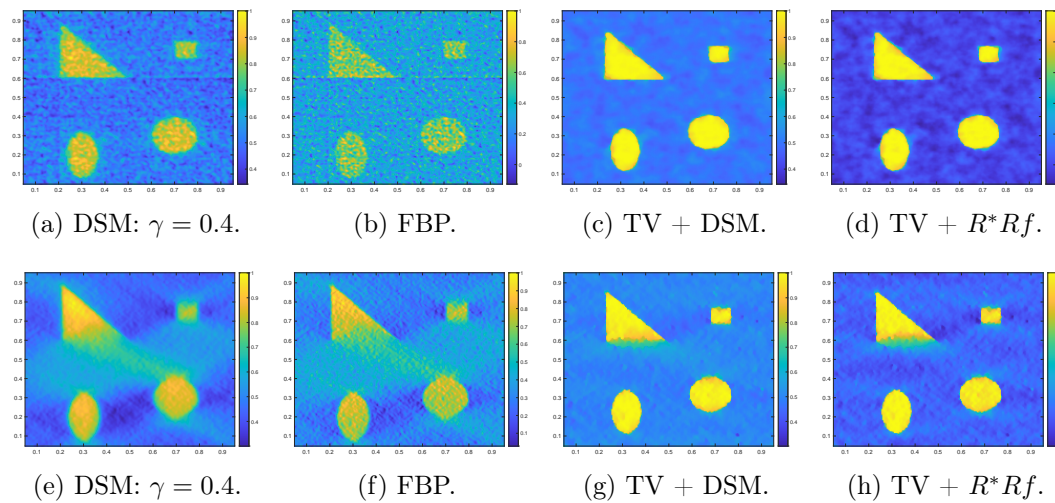


**Figure 8.** Example 5. Reconstruction with 5% additive Gaussian noise for sparse tomography (first row) and limited angle tomography (second row).

Method	MSE	Err $^\infty$	PSNR	SSIM	CPU time (s)	Iterations
DSM	0.152	0.162	21.205	0.464	0.015	/
FBP	0.334	0.452	14.350	0.060	0.016	/
TV + DSM	0.044	0.071	32.045	0.936	1.462	43
TV + $R^*Rf$	0.047	0.073	31.324	0.911	2.486	83

for the reconstruction with projections from 36 angles uniformly distributed in  $(-\pi, \pi]$  (the first row of Figure 8) and

Method	MSE	Err $^\infty$	PSNR	SSIM	CPU time (s)	Iterations
DSM	0.186	0.182	19.434	0.743	0.036	/
FBP	0.282	0.269	15.842	0.228	0.054	/
TV + DSM	0.065	0.092	28.587	0.869	17.013	103
TV + $R^*Rf$	0.072	0.106	27.633	0.825	29.240	191

for the reconstruction with projection angles uniformly distributed in  $[-\pi/3, \pi/3]$  (the second row of Figure 8).

Comparing the reconstructions by DSM and FBP, we see that DSM demonstrates its strong robustness through accurate reconstruction results in the above two scenarios which are consistent with our previous observations. Moreover, it is evident that the direct type methods, i.e., DSM and FBP, are much faster compared with iterative methods regarding the CPU times of reconstruction that can be found in the sixth column of the above table.

By comparing the number of iterations required by minimizing the target functional (with the initial guesses provided by the common choice  $R^*Rf$  and the proposed DSM), we can further observe that the novel DSM helps reduce the number of iterations needed significantly for more than 45%. Hence, the application of DSM as an initial guess for minimizing the least-square functional with TV is attractive in practice.

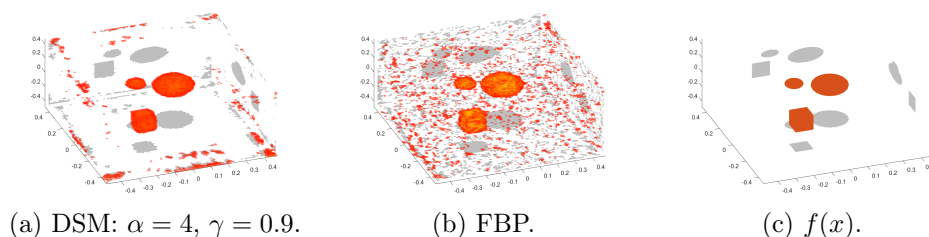


**Figure 9.** Example 6. Reconstruction in  $\mathbb{R}^3$ , with 1% additive Gaussian noise.

*Example 6.* In this example, we consider a three-dimensional reconstruction. The reconstruction by DSM (with  $\alpha = 4$ ,  $\gamma = 0.9$ ) and the FBP method under 1% Gaussian noise are shown in Figure 9, with the mesh size  $h = 10^{-2}$ . For this example, the measurement data is available for 900 discrete angles  $\Gamma_\theta \subset \mathbb{S}^2$  and discrete measurement points  $\Gamma_t(\theta) \subset I_\theta$  as defined in (2.2). We point out that the distribution of measurement angles in this example is relatively sparse considering the difficulty of the three-dimensional reconstruction. The three objects are one rectangular box and two balls located in  $\Omega = [-0.5, 0.5]^3$  as illustrated in Figure 9(a). The target function  $f(x) = 0.5$  if  $x$  lies in these three objects and  $f(x) = 0.3$  otherwise. The corresponding reconstruction errors are given respectively by

Method	MSE	Err $^\infty$	PSNR	SSIM	CPU time (s)
DSM	0.086	0.414	31.696	0.847	3.844
FBP	0.148	0.840	27.005	0.641	3.719

To better illustrate reconstruction results, in Figure 9, supposing  $I_r$  as the reconstructed image by the DSM or the FBP, we set  $I_r(z) = 0$  if  $|I_r(z)| < 0.4$  and  $I_r(z) = 1$  if  $|I_r(z)| \geq 0.4$  for  $z \in \Omega$  to represent the support of objects reconstructed. From Figure 9(a), we see that DSM can recover the basic shape, size, and position of the three objects quite reasonably, with three objects well separated, especially the two balls that are rather close to each other. The reconstruction by the FBP method in Figure 9(b) generates many improper noisy points in the whole sampling domain. This example demonstrates the accuracy of DSM in reconstructing the support of objects in  $\mathbb{R}^3$  with noisy measurement data.

**7. Concluding remarks.** We have proposed a novel stable and fast DSM for the inversion of the Radon transform that can be implemented in a completely parallel manner, which is severely ill-posed when the measurement data is noisy and very limited as it appears frequently in real applications.

The DSM leverages on an important almost orthogonality property under a fractional order duality product. A family of probing functions is constructed by modifying the Green's function associated with a related fractional Laplacian. As a result of the choices of the appropriate duality product space and probing functions, the novel DSM can generate fast and satisfactory reconstruction results in challenging cases when the measurement data is highly noisy and limited. So DSM may have good potential applications in many real scenarios, such as security scanning, cancer detection, portable CT scanners, and so on.

Along this research direction, there are several important topics that are worth exploring in the future. For instance, a more systematic derivation and optimal choice of other effective probing functions are very interesting and can provide more concrete guidance in practice when DSM is applied. Moreover, the validation of the DSM for the sparse tomography and the limited angle tomography are also very important due to the wide applications of these imaging techniques. From our analyses in this work, it is feasible to generalize direct sampling type methods to many other tomography problems, for instance, the general exponential Radon transform, cone-beam CT, the geodesic Radon transform, and so on. In the meantime, the generalization should preserve nice features similar to the ones of DSM in this work.

**Appendix A. Choice of the smooth extension function  $\psi_{n+1}$  in (2.8).** In this appendix, we shall present our choice of the smooth extension function  $\psi_{n+1}$  in the definition of the auxiliary function  $\zeta_{n+1}^h$  (2.7) which is further employed to define the crucial probing function in (2.8). We shall point out that the smooth extension function for other choices  $\alpha$  in (2.7) can be constructed similarly.

We notice that, to allow  $\zeta_{n+1}^h$  to possess desired properties stated in (2.7), it is sufficient to require  $\psi_{n+1} : [0, h] \rightarrow \mathbb{R}$  to satisfy

$$(A.1) \quad \psi_{n+1} \in C^{2,1}([0, h]); \quad \begin{cases} \psi_{n+1}(h) = h^{-n-1}, \\ \psi'_{n+1}(h) = -(n+1)h^{-n-2}, \\ \psi''_{n+1}(h) = (n+1)(n+2)h^{-n-3}; \end{cases} \quad \begin{cases} \psi_{n+1}(0) = h^{-n}, \\ \psi'_{n+1}(0) = 0, \\ \psi''_{n+1}(0) = 0; \end{cases}$$

and for  $B(0, h) \subset \mathbb{R}^n$  and  $h < 1$ ,

$$(A.2) \quad \int_{B(0, h)} |\psi_{n+1}(|x|) - h^{-n-1}| dx \leq h.$$

Our choice of  $\psi_{n+1}(t)$  is to construct a polynomial that matches desired boundary conditions when  $t = h$  and  $t = 0$  in (A.1), and then we restrict the support of the function  $\psi_{n+1}(t) - h^{-n-1}$  to meet the requirement (A.2). For simplicity, we write  $k = n + 1$  and  $b = h - h^2/n$ , then  $\psi_k(t)$  is defined as

$$(A.3) \quad \begin{aligned} \psi_k(t) := & \frac{1}{h^k} \left[ 1 + \left( \frac{k^2 + k}{2h^4} + \frac{4k}{h^5} \right) (t - b)^3 - \frac{1}{h^2} \left( \frac{k^2 + k}{h^4} + \frac{7k}{h^5} \right) (t - b)^4 \right. \\ & \left. + \frac{1}{h^4} \left( \frac{k^2 + k}{2h^4} + \frac{3k}{h^5} \right) (t - b)^5 \right] \end{aligned}$$

for  $t \in [b, h]$ , and  $\psi_k(t) := 0$  for  $t \in [0, b)$ .

Therefore, the first and second order derivatives of  $\psi_k(t)$  for  $t \in [b, h]$  are

$$\begin{aligned} \psi'_k(t) &= \frac{1}{h^k} \left[ 3 \left( \frac{k^2 + k}{2h^4} + \frac{4k}{h^5} \right) (t - b)^2 - \frac{4}{h^2} \left( \frac{k^2 + k}{h^4} + \frac{7k}{h^5} \right) (t - b)^3 + \frac{5}{h^4} \left( \frac{k^2 + k}{2h^4} + \frac{3k}{h^5} \right) (t - b)^4 \right], \\ \psi''_k(t) &= \frac{1}{h^k} \left[ 6 \left( \frac{k^2 + k}{2h^4} + \frac{4k}{h^5} \right) (t - b) - \frac{12}{h^2} \left( \frac{k^2 + k}{h^4} + \frac{7k}{h^5} \right) (t - b)^2 + \frac{20}{h^4} \left( \frac{k^2 + k}{2h^4} + \frac{3k}{h^5} \right) (t - b)^3 \right]. \end{aligned}$$

In this case, it is straightforward to verify that  $\psi_k(t)$  satisfies (A.1).

To show that the condition (A.2) is satisfied by  $\psi_k$ , we first notice, for  $t \in [b, h]$ ,  $\psi_k(t) - h^{-k}$  equals to

$$\psi_k(t) - \frac{1}{h^k} = \frac{(t-b)^3}{h^k} \left( \frac{t-b}{h} - 1 \right) \left[ \left( \frac{k^2+k}{2h^4} + \frac{3k}{h^5} \right) \left( \frac{t-b}{h} \right) - \left( \frac{k^2+k}{2h^4} + \frac{4k}{h^5} \right) \right].$$

The above shows  $\psi_k(t) - h^{-k} > 0$  for  $t \in [0, h]$ . We now integrate  $\psi_k(|x|) - h^{-k}$  directly by replacing  $t - b$  by  $\tau$ :

$$\begin{aligned} \int_{B(0,h)} \left| \psi_k(|x|) - \frac{1}{h^k} \right| dx &= |S_{n-1}| \int_{h-\frac{h^2}{n}}^h t^{n-1} \frac{(t-b)^3}{h^k} \left( \frac{t-b}{h} - 1 \right) \left[ \left( \frac{k^2+k}{2h^4} + \frac{3k}{h^5} \right) \left( \frac{t-b}{h} \right) - \left( \frac{k^2+k}{2h^4} + \frac{4k}{h^5} \right) \right] dt \\ &= \frac{|S_{n-1}|}{h^{k+2}} \int_0^{\frac{h^2}{n}} (\tau+h-\frac{h^2}{n})^{n-1} \tau^3 (\tau-h) \left[ \left( \frac{k^2+k}{2h^4} + \frac{3k}{h^5} \right) \tau - \left( \frac{k^2+k}{2h^4} + \frac{4k}{h^5} \right) h \right] d\tau. \end{aligned}$$

As  $h < 1$ , for  $n = 2$ , we have

$$\int_{B(0,h)} \left| \psi_k(|x|) - \frac{1}{h^k} \right| dx = \frac{h\pi}{13440} (-30h^4 + 473h^3 - 294h^2 - 3612h + 5040) < \frac{h\pi}{13340} (473 + 5040) < h;$$

and for  $n = 3$ , we have

$$\begin{aligned} \int_{B(0,h)} \left| \psi_k(|x|) - \frac{1}{h^k} \right| dx &= \frac{h\pi}{688905} (25h^5 - 810h^4 + 10914h^3 - 41076h^2 + 3402h + 136080) \\ &\leq \frac{h\pi}{688905} (25 + 10914 + 3402 + 136080) < h. \end{aligned}$$

We have verified that our choice of  $\psi_{n+1}(t)$  in (A.3) satisfies the requirements (A.1) and (A.2) which are a proper candidate to be employed in the numerical computation.

## REFERENCES

- [1] M. ABRAMOWITZ AND I. A. STEGUN, *Handbook of Mathematical Functions, with Formulas, Graphs, and Mathematical Tables*, Dover Publications, New York, 1974.
- [2] A. H. ANDERSEN AND A. C. KAK, *Simultaneous algebraic reconstruction technique (SART): A superior implementation of the art algorithm*, *Ultrason. Imaging*, 6 (1984), pp. 81–94.
- [3] M. BEISTER, D. KOLDITZ, AND W. A. KALENDER, *Iterative reconstruction methods in x-ray CT*, *Phys. Med.*, 28 (2012), pp. 94–108.
- [4] E. J. CANDÈS, J. ROMBERG, AND T. TAO, *Robust uncertainty principles: Exact signal reconstruction from highly incomplete frequency information*, *IEEE Trans. Inform. Theory*, 52 (2006), pp. 489–509.
- [5] R. CHARTRAND, *Exact reconstruction of sparse signals via nonconvex minimization*, *IEEE Signal Process. Lett.*, 14 (2007), pp. 707–710.
- [6] Y. CHEN, J. MA, Q. FENG, L. LUO, P. SHI, AND W. CHEN, *Nonlocal prior Bayesian tomographic reconstruction*, *J. Math. Imaging Vision*, 30 (2008), pp. 133–146.
- [7] Z. CHEN, X. JIN, L. LI, AND G. WANG, *A limited-angle CT reconstruction method based on anisotropic tv minimization*, *Phys. Med. Biol.*, 58 (2013), p. 2119.
- [8] Y. T. CHOW, K. ITO, K. LIU, AND J. ZOU, *Direct sampling method for diffusive optical tomography*, *SIAM J. Sci. Comput.*, 37 (2015), pp. A1658–A1684.
- [9] Y. T. CHOW, K. ITO, AND J. ZOU, *A direct sampling method for electrical impedance tomography*, *Inverse Problems*, 30 (2014), 095003.
- [10] Y. T. CHOW, K. ITO, AND J. ZOU, *A time-dependent direct sampling method for recovering moving potentials in a heat equation*, *SIAM J. Sci. Comput.*, 40 (2018), pp. A2720–A2748.

- [11] M. E. DAVISON, *The ill-conditioned nature of the limited angle tomography problem*, SIAM J. Appl. Math., 43 (1983), pp. 428–448.
- [12] A. H. DELANEY AND Y. BRESLER, *Globally convergent edge-preserving regularized reconstruction: An application to limited-angle tomography*, IEEE Trans. Image Process., 7 (1998), pp. 204–221.
- [13] M. FALL, *Entire  $s$ -harmonic functions are affine*, Proc. Amer. Math. Soc., 144 (2016), pp. 2587–2592.
- [14] J. FRIKEL AND E. T. QUINTO, *Characterization and reduction of artifacts in limited angle tomography*, Inverse Problems, 29 (2013), 125007.
- [15] R. GORDON, R. BENDER, AND G. T. HERMAN, *Algebraic reconstruction techniques (art) for three-dimensional electron microscopy and x-ray photography*, J. Theoret. Biol, 29 (1970), pp. 471–481.
- [16] K. HÄMÄLÄINEN, A. KALLONEN, V. KOLEHMAINEN, M. LASSAS, K. NIINIMÄKI, AND S. SILTANEN, *Sparse tomography*, SIAM J. Sci. Comput., 35 (2013), pp. B644–B665.
- [17] S. HELGASON, *The Radon Transform*, Progr. Math. 5, Birkhäuser Basel, Basel, 1999.
- [18] H. M. HUDSON AND R. S. LARKIN, *Accelerated image reconstruction using ordered subsets of projection data*, IEEE Trans. Med. Imaging, 13 (1994), pp. 601–609.
- [19] K. ITO, B. JIN, AND J. ZOU, *A direct sampling method to an inverse medium scattering problem*, Inverse Problems, 28 (2012), 025003.
- [20] T. L. JENSEN, J. H. JØRGENSEN, P. C. HANSEN, AND S. H. JENSEN, *Implementation of an optimal first-order method for strongly convex total variation regularization*, BIT, 52 (2012), pp. 329–356.
- [21] A. C. KAK AND M. G. SLANEY, *Principles of Computerized Tomography*, Classics in Appl. Math. 33, SIAM, Philadelphia, 1988.
- [22] A. KATSEVICH, *Theoretically exact filtered backprojection-type inversion algorithm for spiral CT*, SIAM J. Appl. Math., 62 (2002), pp. 2012–2026.
- [23] M. KWAŚNICKI, *Ten equivalent definitions of the fractional Laplace operator*, Fract. Calc. Appl. Anal., 20 (2017), pp. 7–51.
- [24] N. S. LANDKOF, *Foundations of Modern Potential Theory*, Grundlehren Math. Wiss. 180, Springer-Verlag, Berlin, 1972.
- [25] J. LI AND J. ZOU, *A direct sampling method for inverse scattering using far-field data*, Inverse Probl. Imaging, 7 (2013), pp. 757–775.
- [26] H. LU, T. HSIAO, X. LI, AND Z. LIANG, *Noise properties of low-dose CT projections and noise treatment by scale transformations*, IEEE Nucl. Sci., 3 (2001), pp. 1662–1666.
- [27] F. NATTERER AND F. WÜBBELING, *Mathematical Methods in Image Reconstruction*, SIAM, Philadelphia, 2001.
- [28] J. D. PACK, F. NOO, AND R. CLACKDOYLE, *Cone-beam reconstruction using the backprojection of locally filtered projections*, IEEE Trans. Med. Imaging, 24 (2005), pp. 70–85.
- [29] X. PAN, E. Y. SIDKY, AND M. VANNIER, *Why do commercial CT scanners still employ traditional, filtered back-projection for image reconstruction?*, Inverse Problems, 25 (2009), 1230009.
- [30] R. POTTHAST, *A study on orthogonality sampling*, Inverse Problems, 26 (2010), 074015.
- [31] M. RANTALA, S. VANSKA, S. JARVENPAA, M. KALKE, M. LASSAS, J. MOBERG, AND S. SILTANEN, *Wavelet-based reconstruction for limited-angle X-ray tomography*, IEEE Trans. Med. Imaging, 25 (2006), pp. 210–217.
- [32] L. RITSCHL, F. BERGNER, C. FLEISCHMANN, AND M. KACHELRIESS, *Improved total variation-based CT image reconstruction applied to clinical data*, Phys. Med. Biol., 56 (2011), pp. 1545–1561.
- [33] L. A. SHEPP AND B. F. LOGAN, *The Fourier reconstruction of a head section*, IEEE Trans. Nucl. Sci., 21 (1974), pp. 21–43.
- [34] L. A. SHEPP AND Y. VARDI, *Maximum likelihood reconstruction for emission tomography*, IEEE Trans. Med. Imaging, 1 (1982), pp. 113–122.
- [35] L. E. SILVESTRE, *Regularity of the obstacle problem for a fractional power of the Laplace operator*, Commun. Pure Appl. Math., 60 (2007), pp. 67–112.
- [36] THE NATIONAL LUNG SCREENING TRIAL RESEARCH TEAM, *Reduced lung-cancer mortality with low-dose computed tomographic screening*, New England J. Med., 365 (2011), pp. 395–409.
- [37] O. TRETIAK AND C. METZ, *The exponential radon transform*, SIAM J. Appl. Math., 39 (1980), pp. 341–354.
- [38] G. WAHBA, *Ill Posed Problems: Numerical and Statistical Methods for Mildly, Moderately and Severely Ill Posed Problems with Noisy Data*, Tech. report, Department of Statistics, Wisconsin University, Madison, 1980.